

1 **Assessing improvements in global ocean pCO₂ machine learning reconstructions with**
2 **Southern Ocean autonomous sampling**

3 Thea H. Heimdal¹, Galen A. McKinley¹, Adrienne J. Sutton², Amanda R. Fay¹, Lucas Gloege³

4 ¹Columbia University and Lamont-Doherty Earth Observatory, Palisades, NY, USA

5 ²Pacific Marine Environmental Laboratory, National Oceanic and Atmospheric Administration,
6 Seattle, WA, USA

7 ³Open Earth Foundation, Marina del Rey, CA, USA

8 *Correspondence to:* Thea H. Heimdal (theimdal@ldeo.columbia.edu)

9

10 **Abstract**

11 The Southern Ocean plays an important role in the exchange of carbon between the atmosphere
12 and oceans, and is a critical region for the ocean uptake of anthropogenic CO₂. However, estimates
13 of the Southern Ocean air-sea CO₂ flux are highly uncertain due to limited data coverage. Increased
14 sampling in winter and across meridional gradients in the Southern Ocean may improve machine
15 learning (ML) reconstructions of global surface ocean pCO₂. Here, we use a Large Ensemble
16 Testbed (LET) of Earth System Models and the pCO₂-Residual reconstruction method to assess
17 improvements in pCO₂ reconstruction fidelity that could be achieved with additional autonomous
18 sampling in the Southern Ocean added to existing Surface Ocean CO₂ Atlas (SOCAT)
19 observations. The LET allows for a robust evaluation of the skill of pCO₂ reconstructions in space
20 and time through comparison to ‘model truth’. With only SOCAT sampling, Southern Ocean and
21 global pCO₂ are overestimated, and thus the ocean carbon sink is underestimated. Incorporating
22 Uncrewed Surface Vehicle (USV) sampling increases the spatial and seasonal coverage of
23 observations within the Southern Ocean, leading to a decrease in the overestimation of pCO₂. A
24 modest number of additional observations in southern hemisphere winter and across meridional
25 gradients in the Southern Ocean leads to improvement in reconstruction bias and root-mean
26 squared error (RMSE) by as much as 95 % and 16 %, respectively, as compared to SOCAT
27 sampling alone. Lastly, the large decadal variability of air-sea CO₂ fluxes shown by SOCAT-only
28 sampling may be partially attributable to undersampling of the Southern Ocean.

29

30 1. Introduction

31 The ocean plays an important role in mitigating climate change by sequestering anthropogenic
32 carbon emissions. From 1850 to 2023, the oceans have removed a total of 180 ± 35 Gt of carbon
33 (Friedlingstein et al., 2023). In order to fully understand the climate impacts from rising emissions,
34 it is essential to accurately quantify the air-sea CO_2 flux and the global ocean carbon sink in space
35 and time. The Surface Ocean CO_2 Atlas (SOCAT; Bakker et al., 2016) is the largest global
36 database of surface ocean CO_2 observations, with data starting in 1957. The main synthesis and
37 gridded products contain over 33 million high-quality direct shipboard measurements of $f\text{CO}_2$
38 (fugacity of CO_2) with an uncertainty of $< 5 \mu\text{atm}$ (Bakker et al., 2022). However, due to limited
39 resources for ocean observing, limited number of ships/routes, inaccessible regions and unsafe
40 waters, the database covers only about 1% of the global ocean at monthly $1^\circ \times 1^\circ$ spatial resolution
41 over the period of 1982-2023, and is highly biased towards the northern hemisphere.

42 Observation-based data products have been developed to estimate full-coverage surface
43 ocean $p\text{CO}_2$ across space and time by extrapolating to global coverage from these sparse SOCAT
44 observations (e.g., Landschützer et al., 2014; Rödenbeck et al., 2015; Gloege et al., 2022;
45 Bennington et al., 2022a,b). Most of these data products utilize machine learning (ML) algorithms
46 to estimate a non-linear function between a suite of driver variables (i.e., sea surface temperature
47 - SST, sea surface salinity - SSS, mixed layer depth - MLD, Chlorophyll - Chl-a, $x\text{CO}_2$ -
48 atmospheric CO_2) and surface ocean $p\text{CO}_2$ (the target variable) where these are co-located. The
49 driver variables are proxies for processes influencing ocean $p\text{CO}_2$. Full-coverage driver variable
50 datasets are then processed through these ML algorithms to produce estimated global full-coverage
51 surface ocean $p\text{CO}_2$. Since the data products rely on $p\text{CO}_2$ observations to estimate functions
52 between the target and driver variables, data sparsity remains a fundamental limitation to this
53 technique.

54 It has been suggested that targeted sampling from autonomous platforms combined with
55 ships, filling in the state space of $p\text{CO}_2$, represents a path forward to improve surface ocean $p\text{CO}_2$
56 reconstructions (Bushinsky et al., 2019; Gregor et al., 2019; Gloege et al., 2021; Djeutchouang et
57 al., 2022; Landschützer et al., 2023; Hauck et al., 2023). One major obstacle, however, is that the
58 indirect $p\text{CO}_2$ estimates from floats have high uncertainties ($\pm 11.4 \mu\text{atm}$) and may be biased by
59 as much as $\sim 4 \mu\text{atm}$ (Bakker et al., 2016; Williams et al., 2017; Fay et al., 2018; Gray et al., 2018;

60 Sutton et al., 2021; Mackay and Watson 2021; Wu et al 2022). These large uncertainties and biases
61 arise when pCO₂ is not measured directly as in the observations included in SOCAT, but is rather
62 estimated using measurements of pH combined with a regression-derived alkalinity estimate
63 (Williams et al., 2017; Gray et al., 2018). SOCAT includes only direct pCO₂ observations. Biases
64 and uncertainties may have large impacts on global air-sea CO₂ flux estimates, given that the global
65 mean air-sea disequilibrium is only 5-8 μatm (McKinley et al., 2020). It is therefore critical that
66 bias and uncertainty corrections are well-constrained over different oceanic conditions and over
67 time.

68 Uncrewed Surface Vehicles (USVs), such as those manufactured and maintained by
69 Saildrone Inc., represent a new type of autonomous platform that can obtain direct pCO₂
70 observations with significantly lower uncertainties compared to other autonomous methods, and
71 equivalent to the highest-quality shipboard measurements contained in SOCAT (± 2 μatm; Sabine
72 et al., 2020; Sutton et al., 2021). Such improvements in sampling are critically important in the
73 undersampled Southern Ocean. This region is fundamental in terms of the ocean's ability to
74 remove carbon from the atmosphere, being responsible for ~ 40% of the global ocean uptake of
75 anthropogenic CO₂ (Khatiwala et al., 2009). Improved data coverage in the Southern Ocean
76 represents thus a major opportunity to advance our understanding of the global ocean carbon sink
77 (Lenton et al., 2006, 2013; Takahashi et al., 2009; Monteiro et al., 2015; Gregor et al., 2019; Gray
78 et al., 2018; Mongwe et al., 2018; Bushinsky et al., 2019; Sutton et al., 2021; Long et al., 2021;
79 Mackay et al., 2022; Wu et al., 2022; Landschützer et al., 2023; Hauck et al., 2023). A combination
80 of SOCAT and Saildrone USV observations would include high-accuracy data from both the long
81 record and global coverage of ship tracks, and the expanded finer resolution of spatial and seasonal
82 coverage of the poorly sampled Southern Ocean. Importantly, Saildrone USVs are also able to
83 cover the spatial extent and seasonal cycle of the meridional gradients, which has been shown to
84 be critical in order to reduce errors in reconstructing surface ocean pCO₂ (Djeutchouang et al.,
85 2022). A combined approach, with autonomous samples such as those obtained from Saildrone
86 USVs, in addition to high-quality observations collected from ships, represents thus a promising
87 solution to improve surface ocean pCO₂ ML reconstructions.

88 Here, we assess to what extent surface ocean pCO₂ reconstructions can improve by
89 implementing the pCO₂-Residual machine learning (ML) reconstruction (Bennington et al., 2022a)

90 with the combined inputs of SOCAT and Saildrone USV coverage. However, instead of using real-
91 world observations, we sample the target (i.e., surface ocean pCO₂) and driver variables (i.e., SST,
92 SSS, MLD, Chl-a and xCO₂) from our Large Ensemble Testbed (LET) of Earth System Models
93 (ESMs) (e.g., Stamell et al., 2020; Gloege et al., 2021; Bennington et al., 2022a). There are two
94 major benefits of using a testbed compared to actual observations. First, in an ESM, the surface
95 ocean pCO₂ field is provided precisely at all model times and 1°x1° points. Therefore, the pCO₂
96 reconstructed by the ML algorithm can be robustly evaluated in space and time against a known
97 ‘truth’ (i.e., ‘model truth’). The reconstruction evaluation is thus not limited to the availability of
98 sparse real-world ocean observations. Secondly, a testbed can be used to plan and evaluate the
99 impact of different sampling strategies on the reconstructed pCO₂. It is important to stress that, by
100 using a model testbed, we do not predict real-world surface ocean pCO₂ and air-sea CO₂ fluxes.
101 The goal here is to assess the accuracy with which an ML algorithm can reconstruct the ‘model
102 truth’ given inputs of samples consistent with real-world data coverage from the SOCAT database
103 and Saildrone USVs.

104 By utilizing the observational coverage of SOCAT and Saildrone USV transects, we assess
105 to what extent the pCO₂-Residual method accurately reconstructs model surface ocean pCO₂ in
106 space and time. Additionally, we explore the timing, magnitude, duration and spatial extent of
107 Southern Ocean USV sample additions that most significantly improve the pCO₂ predictions.

108 **2. Methods**

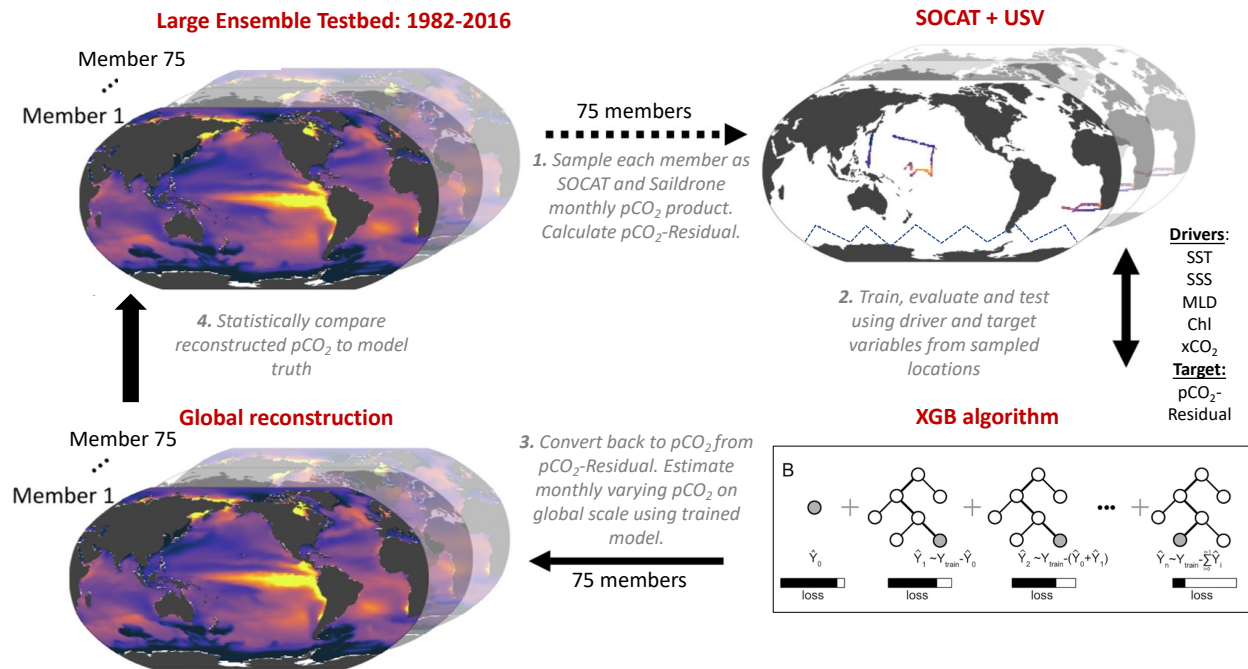
109 *2.1 The Large Ensemble Testbed (LET)*

110 In this study, the Large Ensemble Testbed (LET) includes 25 members from three independent
111 initial-condition ensemble models (i.e., CanESM2, CESM-LENS and GFDL-ESM2M; Kay et al.,
112 2015; Rodgers et al., 2015; Fyfe et al., 2017), giving a total of 75 members within the testbed. We
113 do not use the MPI-GE model that was included in the past LET studies because its Southern
114 Ocean pCO₂ seasonality and decadal variability appear to be anomalously large (Gloege et al.,
115 2021; Fay and McKinley, 2021; Bennington et al., 2022a). Each individual Earth System Model
116 (ESM) is an imperfect representation of the actual Earth system, so the multiple Large Ensembles
117 are used to span different model structures and their representation of internal variability. Each
118 ensemble member undergoes the same external forcing (i.e., historical atmospheric CO₂ before

119 2005 and Representative Concentration Pathway 8.5 through 2016, plus solar and volcanic
 120 forcing), but the spread across the ensemble members gives a unique trajectory of the ocean-
 121 atmosphere state over time, i.e., a different state of internal variability as well as the difference
 122 across models.

123 The LET used in this study includes monthly $1^\circ \times 1^\circ$ model output from 1982-2016 (Gloege
 124 et al., 2021). For each individual ensemble member of the LET, surface ocean $p\text{CO}_2$ and co-located
 125 driver variables (i.e., SST, SSS, Chl-a, MLD, $x\text{CO}_2$) were sampled monthly at a $1^\circ \times 1^\circ$ resolution,
 126 at times and locations equivalent to SOCAT and Saildrone USV observations (**Fig. 1**; Step 1).
 127 While the SOCAT observations were sampled from the testbed matching the actual years of
 128 sampling, the USV observations were sampled from the testbed starting in 2007 (for ten-year
 129 sampling) or 2012 (for five-year sampling) (see **Sect. 2.4**). As our focus is on reconstruction for
 130 the open ocean, testbed output for coastal areas, the Arctic Ocean ($>79^\circ\text{N}$) and marginal seas
 131 (Hudson Bay, Caspian Sea, Black Sea, Mediterranean Sea, Baltic Sea, Java Sea, Red Sea and Sea
 132 of Okhotsk) were removed prior to algorithm processing.

133



134 **Figure 1:** Schematic of the Large Ensemble Testbed (LET; modified from Gloege et al., 2021). **1:** Surface ocean
 135 $p\text{CO}_2$ from each of the 75 model members is sampled in space and time mimicking real-world SOCAT and Saildrone
 136 USV observations (see **Fig. 2**; **Table 1**; **Section 2.5**). Prior to algorithm processing, $p\text{CO}_2$ -Residual is calculated
 137 (**Section 2.2**). **2:** The $p\text{CO}_2$ -Residual (target variable) and co-located driver variables (i.e., SST, SSS, MLD, Chl,
 138

139 xCO₂) sampled from the testbed are processed by the XGBoost (XGB) algorithm (**Section 2.3**). **3:** Based on the full-
140 coverage of driver variables, pCO₂-Residual is reconstructed globally. This process is repeated 75 times, individually
141 for every single testbed model member. The temperature component (pCO₂-T) is then added back to the pCO₂-
142 Residual for each value. **4:** The globally reconstructed pCO₂ is evaluated against the ‘model truth’ at all 1°x1° grid
143 cells. SST = sea surface temperature. SSS = sea surface salinity. MLD = mixed layer depth. Chl = chlorophyll. xCO₂
144 = atmospheric concentration of CO₂.

145

146 *2.2 The pCO₂-Residual approach*

147 We used the pCO₂-Residual approach following Bennington et al. (2022a), which removes the
148 well-studied direct effect of temperature on pCO₂ from the LET model output before algorithm
149 processing. Temperature has both direct and indirect effects on surface ocean pCO₂. The direct
150 effect of temperature, due to solubility and chemical equilibrium, is that an increase in temperature
151 directly causes an increase in pCO₂ (Takahashi et al., 1993). Indirectly, temperature changes are
152 associated with biological production and wintertime vertical mixing; and these processes tend to
153 result in opposing pCO₂ changes. To build reconstruction algorithms through the data-driven
154 training that occurs in ML, the statistics in all other algorithms developed to date must identify a
155 function that disentangles these competing effects of SST on pCO₂. Here, the algorithm is assisted
156 by removing this known temperature effect, and it must therefore only learn the pCO₂ impacts
157 from biogeochemical drivers. The pCO₂-Residual method leads to physically understandable
158 connections between the input data and output (Bennington et al., 2022a), which mitigates to some
159 degree ‘black box’ concerns typically associated with ML algorithms (Toms et al., 2020). Further,
160 this method has been shown to perform better against independent observations than other
161 common observation-based products (Bennington et al., 2022a). A brief description is provided
162 here, but for further details see Bennington et al. (2022a).

163 The temperature-driven component of pCO₂ (pCO₂-T) is calculated using this equation:

$$164 \quad \text{pCO}_2\text{-T} = \text{pCO}_2^{\text{mean}} * \exp[0.0423 * (\text{SST} - \text{SST}^{\text{mean}})]$$

165 where pCO₂^{mean} and SST^{mean} is the long-term mean of surface ocean pCO₂ and temperature,
166 respectively, using all 1°x1° grid cells from the testbed. Once pCO₂-T is determined, pCO₂-
167 Residual is calculated as the difference between pCO₂ and the calculated pCO₂-T:

$$168 \quad \text{pCO}_2\text{-Residual} = \text{pCO}_2 - \text{pCO}_2\text{-T}$$

169 Prior to algorithm processing, pCO₂-Residual values > 250 μatm and < -250 μatm from the
170 testbed were filtered out targeting values that are not representative of the real ocean. The majority
171 of the pCO₂-Residual values that were filtered out correspond to high pCO₂, above the maximum
172 value in SOCAT (816 μatm; Stamell et al., 2020). The excluded data points (less than 0.2 % per
173 member) mostly occurred in output from the CanESM2 model, and were restricted geographically,
174 predominantly along the western coastline of South America.

175 The eXtreme Gradient Boosting method (XGB; Chen and Guestrin, 2016) is used to
176 develop an algorithm that allows driver variables (i.e., SST, SSS, Chl-a, MLD, xCO₂) to predict
177 the pCO₂-Residual (**Fig. 1**; Step 2). The pCO₂-Residual and associated feature variables is split
178 into validation, training and testing sets. The test and validation set each account for 20 % of the
179 data, leaving 60 % for training. The validation set is used to optimize the algorithm
180 hyperparameters, which define the architecture of decision trees used in the model. The training
181 set is used to build the decision trees in XGB, while the test set is used to evaluate the performance
182 of the final algorithm. The XGB algorithm for this study used 4,000 decision trees with a maximum
183 depth of 6 levels, and this was fixed for all experiments. For the final reconstruction of surface
184 ocean pCO₂ across all space and time points, the previously calculated pCO₂-T values are added
185 back to the reconstructed pCO₂-Residual (**Fig. 1**; Step 3).

186 The full XGB process, including 1) training/evaluating/testing and 2) reconstructing
187 globally at a monthly resolution, was repeated individually for each LET member. This process
188 provided therefore a total of 75 unique reconstruction vs. ‘model truth’ pairs, which can be
189 statistically compared (**Fig. 1**; Step 4).

190 *2.3 Statistical Analysis in the Testbed*

191 The statistical comparisons between the test set and the reconstructions are equivalent to what
192 would be derived using real-world data (‘seen’ values). Here, we calculate error statistics based on
193 the full reconstruction (pCO₂ from all 1°x1° grid cells of the testbed, except for those masked or
194 filtered out). In the full reconstruction, ~ 99 % of the data do not correspond to SOCAT or
195 Saildrone USV observations used to train the algorithm (**Fig. S1**). Training data would ideally be
196 removed before performance evaluation, but since the training data represent only ~ 1 %, the
197 impact of not removing them is negligible (**Fig. S2**). A suite of statistical metrics can be used to

198 compare the reconstruction to the ‘model truth’ in order to assess how well the algorithm can
199 extrapolate from sparse data to full-field coverage (**Fig. 1**; Step 4). In this study, we focus on bias
200 and root-mean-squared error (RMSE). Bias is calculated as ‘mean prediction – mean observation’
201 (i.e., pCO₂ predicted by XGB subtracted by the pCO₂ ‘model truth’), and is a measure of over- or
202 underestimation in the reconstructions. RMSE measures the magnitude of the predicted error and
203 is calculated as the square root of the mean of the squared errors. We focus our discussion on the
204 mean across 75 members of the testbed for bias and RMSE. The spread across testbed ensemble
205 members is non-negligible and will be the focus of future work; here, we present the testbed spread
206 primarily in the **Supplement**.

207 *2.4 Overview of sampling patterns and model runs*

208 First, we sampled target and driver variables from the LET based on sampling distributions
209 equivalent to that of the SOCAT database (‘SOCAT-baseline’). Then, we combined the ‘SOCAT-
210 baseline’ with testbed output representing additional Saildrone USV coverage in the Southern
211 Ocean. The additional Southern Ocean coverage was based on 1) the Sutton et al. (2021) sampling
212 campaign from 2019 (‘one-latitude’ track) and 2) realistic potential future meridional USV
213 observations (‘zigzag’ track) (see **Section 2.4.2**; **Fig. 2**). We performed a total of 10 experimental
214 runs (**Table 1**). These represent different sampling approaches, including: 1) repeating USV
215 sampling over a five- or ten-year period, 2) varying the number of USVs and thus the total number
216 of monthly 1°x1° observations, and 3) restricting all observations to southern hemisphere winter
217 months. By comparing the different runs, we can assess whether or not certain targeted sampling
218 strategies in the Southern Ocean can improve surface ocean pCO₂ ML reconstructions. As
219 discussed above, the LET runs to 2016 only (Gloege et al., 2021). Saildrone USV observations
220 were therefore sampled from the testbed starting in year 2006 or 2007 (for the ten-year sampling)
221 or 2012 (for the five-year sampling) until 2016, i.e., the final year of the testbed.

222 *2.4.1 ‘One-latitude’ runs*

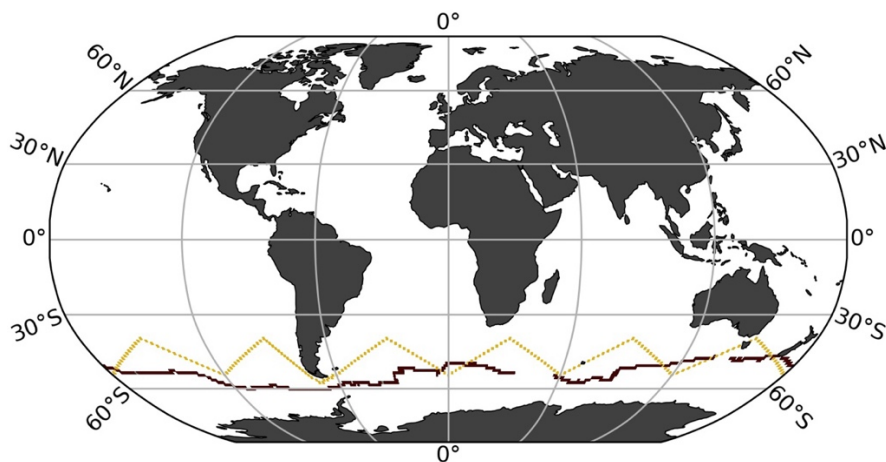
223 Six out of the ten experimental runs include the ‘one-latitude’ track (**Table 1**). The 2019 Saildrone
224 USV journey (Sutton et al., 2021) covered an 8-month period, from January to August. Since the
225 USV was recovered in early August, it did not cover the entire southern hemisphere winter (**Fig.**
226 **S3**). We repeated this ‘one-latitude’ eight-month sampling pattern for five years (‘5Y_J-A’; 2,075

227 observations) and ten years ('10Y_J-A'; 4,150 observations). To evaluate year-round ('YR')
228 coverage, the eight-month sampling period (January-August) was shifted by one month each year
229 for ten years ('10Y_YR'; 4,150 observations). To evaluate the impact of increased sampling, the
230 2019 Saildrone USV track was repeated 12 times with incremental offsets of 1° from the original
231 track, covering an additional 6° north and south (**Fig. S4**). This 'high-sampling'-run ('x13_10Y_J-
232 A'; 44,250 observations) represents a total of 13 USVs. We also performed an additional 13 USV
233 run, but including observations from southern hemisphere winter ('W') months only
234 ('x13_10Y_W'; 25,395 observations). Finally, considering the cost of deploying 13 USVs, a
235 downscaled 'multiple-USV-winter-only'-run was tested, including five USVs sampling over a
236 period of five years ('x5_5Y_W'; 5,022 observations). This run covers an additional 2° north and
237 south from the original USV track.

238 2.4.2 'Zigzag' runs

239 Four of the ten experimental runs represent realistic potential meridional sampling in the Southern
240 Ocean ('zigzag' tracks; **Table 1**) as suggested by Djeutchouang et al. (2022). Saildrone USVs can
241 operate at a speed capable of covering the spatial extent of meridional gradients in the Southern
242 Ocean (Djeutchouang et al., 2022). However, Saildrone USVs are solar powered, and thus their
243 range is restricted by the availability of solar radiation. To account for this and maintain a realistic
244 sampling scenario, sampling occurs only to a maximum latitude of 55° S in these experiments.
245 This alternative sampling pattern represents USVs sailing west to east in a north/south 'zigzag'
246 pattern covering 40° S and 55° S for every 30° of longitude (**Fig. 2**). We created two scenarios.
247 For the first scenario, every 30° of longitude from 40° S and 55° S is visited every three months
248 within a single year as suggested by Lenton et al. (2006). Assuming an average Saildrone USV
249 speed, this scenario represents four platforms equally spaced around the Southern Ocean. This
250 sampling pattern was repeated for 10 years, with year-round coverage ('Zx4_10Y_YR'; 7,600
251 observations), and for southern hemisphere winter months only ('Zx4_10Y_W'; 2,500
252 observations). The second scenario represents a 'high-sampling' strategy, where every 30° of
253 longitude from 40° S and 55° S is visited approximately monthly. This can be achieved by
254 deploying 10 platforms equally spaced around the Southern Ocean running at an average Saildrone
255 USV speed. This sampling pattern is repeated for five years, sampling year-round

256 ('Z_x10_5Y_YR'; 11,400 observations) and during southern hemisphere winter months only
 257 ('Z_x10_5Y_W'; 3,800 observations).



258
 259 **Figure 2:** SAILDRONE Uncrewed Surface Vehicle (USV) tracks representing the first circumnavigation around
 260 Antarctica from 2019 in maroon ('one-latitude' track; Sutton et al., 2021) and an alternative virtual route with
 261 meridional coverage ('zigzag' track).

Run name	SOCAT-baseline	5Y J-A	10Y J-A	10Y YR	x13 10Y J-A	x13 10Y W	x5 5Y W	Z x4 10Y YR	Z x4 10Y W	Z x10 5Y YR	Z x10 5Y W
Saildrone track	NA	One-lat	One-lat	One-lat	One-lat	One-lat	One-lat	Zigzag	Zigzag	Zigzag	Zigzag
Years of sampling	NA	5	10	10	10	10	5	10	10	5	5
Duration of sampling	NA	Jan-Aug	Jan-Aug	Year-round	Jan-Aug	SO winter	SO winter	Year-round	SO winter	Year-round	SO winter
Additional observations	NA	2,075	4,150	4,150	44,250	25,395	5,022	7,600	2,500	11,400	3,800
Global coverage increase (%)	NA	0.01	0.02	0.02	0.3	0.1	0.03	0.04	0.01	0.07	0.02
Mean bias (μatm)											
<i>Testbed period (1982-2016)</i>											
Globally	0.63	0.59	0.59	0.52	0.53	0.39	0.57	0.51	0.51	0.45	0.44
NORTH (35°N-90°N)	0.11	0.24	0.20	0.25	0.20	0.17	0.16	0.16	0.16	0.12	0.20
MID (35°S-35°N)	0.23	0.21	0.22	0.14	0.20	0.15	0.23	0.20	0.18	0.13	0.18
SOUTH (90°S-35°S)	1.4	1.3	1.2	1.1	1.1	0.80	1.2	1.1	1.1	1.0	0.87
SO winter months (JJA)	1.3	1.2	1.2	1.1	1.1	0.90	1.2	0.93	1.0	0.94	0.95
SO summer months (DJF)	0.070	0.11	0.15	0.10	0.15	0.019	0.11	0.25	0.073	0.16	0.066
<i>2006/2012-2016</i>											
Globally	0.51*	0.27	0.34	0.28	0.19	0.03	0.21	0.23	0.24	0.17	0.07
SOUTH (90°S-35°S)	1.6*	0.93	1.1	1.0	0.72	0.37	0.73	0.89	0.92	0.67	0.55
SOUTH (90°S-35°S) Jun, Jul, Aug	4.2*	2.6	2.7	2.8	2.2	1.8	2.5	1.8	2.4	1.2	2.0
Mean RMSE (μatm)											
<i>Testbed period (1982-2016)</i>											
Globally	11.8	11.7	11.8	11.7	11.7	11.6	11.7	11.5	11.6	11.5	11.6
NORTH (35°N-90°N)	13.0	13.0	13.0	13.0	13.0	13.0	13.1	13.0	13.0	13.0	13.0
MID (35°S-35°N)	11.7	11.7	11.7	11.7	11.7	11.7	11.7	11.7	11.7	11.7	11.7
SOUTH (90°S-35°S)	11.5	11.3	11.4	11.2	11.1	11.0	11.3	10.7	11.0	10.6	11.0
<i>2006/2012-2016</i>											
Globally	11.6*	11.6	11.4	11.3	11.3	11.2	11.6	11.0	11.2	11.1	11.4
SOUTH (90°S-35°S)	11.4*	11.1	11.0	10.7	10.6	10.4	10.9	10.0	10.6	9.7	10.6
SOUTH (90°S-35°S) Jun, Jul, Aug	12.0*	11.3	11.2	10.9	10.5	10.3	11.1	10.3	10.6	9.6	10.3

262
 263 **Table 1.** Overview of the different sampling experiments tested in this study, and mean bias and RMSE (in μatm) for
 264 various time periods, latitude bands for all runs. Bold values represent the best score for each category. 'One-lat' =
 265 'one-latitude' track; incorporates the SAILDRONE USV route from Sutton et al. (2021). 'Zigzag' = potential meridional
 266 sampling. 'Additional observations' = number of $1^\circ \times 1^\circ$ monthly SAILDRONE USV observations in addition to SOCAT.
 267 J-A = January-August. YR = year-round. W = southern hemisphere winter. x4, x5, x10 and x13 = four, five, ten and
 268 13 USVs. SO winter = Southern Ocean winter months, i.e., June, July, August and also including September. *Average
 269 value of the mean of 2006-2016 and 2012-2016. The global coverage increase was calculated based on the total
 270 number of available 1982-2016 monthly $1^\circ \times 1^\circ$ observations from SOCAT (262,204 observations) and the Large
 271 Ensemble Testbed (17,290,470 observations).

272

273 **2.5 Air-sea CO_2 flux**

274 To assess the global ocean carbon sink associated with our pCO₂ reconstructions, air-sea CO₂
275 exchange was calculated for 1985 onward. Here, we computed air-sea CO₂ fluxes using the bulk
276 formulation with python package Seaflux.1.3.1 (<https://github.com/lukegre/SeaFlux>; Gregor et al.
277 2021; Fay et al., 2021). We calculated global and Southern Ocean flux in the same manner for 1)
278 the testbed ‘model truth’, 2) the ‘SOCAT-baseline’ and 3) the 10 experimental USV runs.

279 The net sea–air CO₂ flux was estimated using:

$$280 \text{ Flux} = k_w \cdot \text{sol} \cdot (\text{pCO}_2^{\text{ocn}} - \text{pCO}_2^{\text{atm}}) \cdot (1 - \text{ice})$$

281 where ‘k_w’ is the gas transfer velocity, ‘sol’ is the solubility of CO₂ in seawater (in units of mol
282 m⁻³ μatm⁻¹), ‘pCO₂^{ocn}’ is the partial pressure of surface ocean carbon (in μatm), either from the
283 ‘model truth’ or from the reconstructions, and pCO₂^{atm} (in μatm) is the partial pressure of
284 atmospheric CO₂ in the marine boundary layer. For GFDL, we used direct model output of
285 pCO₂^{atm}, while for CESM and CanESM2, pCO₂^{atm} was calculated individually, as the product of
286 surface xCO₂ and sea level pressure (the contribution of water vapor pressure was corrected for in
287 CESM and GFDL). Finally, to account for the seasonal ice cover in high latitudes, the fluxes were
288 weighted by 1 minus the ice fraction (‘ice’), i.e., the open ocean fraction. Inputs to the calculation
289 include EN4.2.2 salinity (Good et al., 2013), SST and ice fraction from NOAA Optimum
290 Interpolation Sea Surface Temperature V2 (OISSTv2) (Reynolds et al., 2002), and surface winds
291 and associated wind scaling factor from the European Centre for Medium-Range Weather
292 Forecasts (ECMWF ERA5 sea level pressure (Hersbach et al., 2020). Results presented show the
293 global and Southern Ocean (< 35° S) fluxes in units of Pg C yr⁻¹.

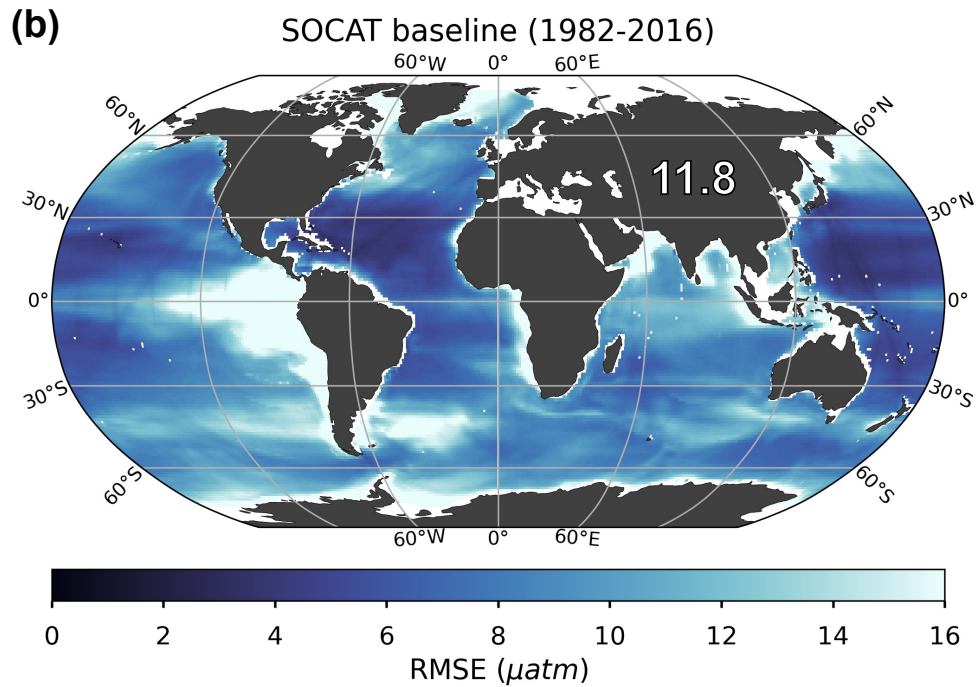
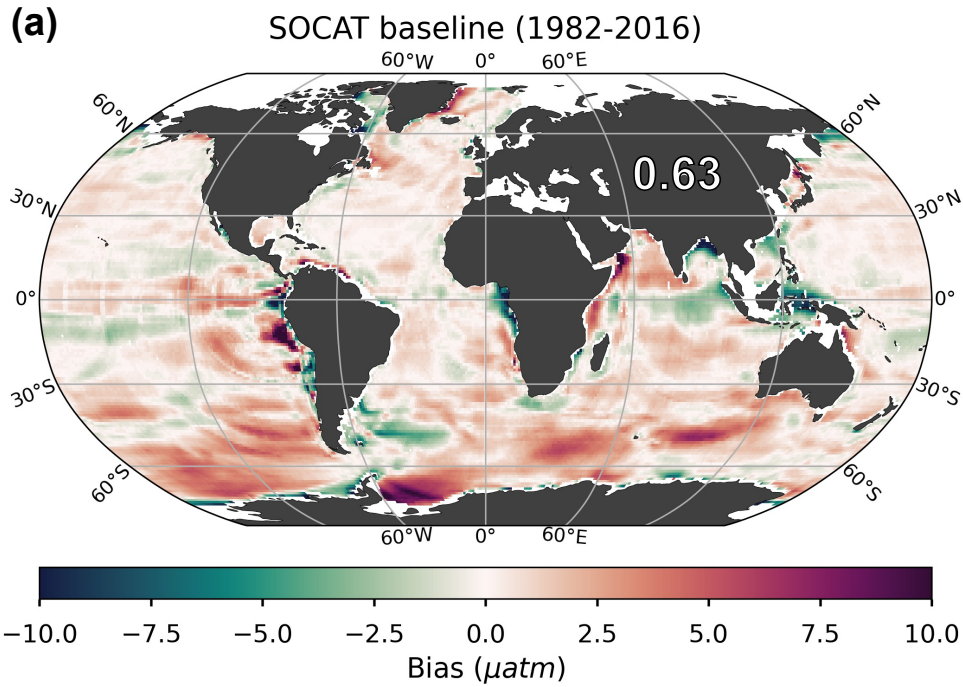
294 Note that, reconstructions of pCO₂ for the ‘SOCAT-baseline’ and the experimental USV
295 runs are limited in their spatial extent to the open ocean (see **Sect. 2.1**; excluding coastal areas, the
296 Arctic Ocean and marginal seas). The same mask was thus also applied when calculating the flux
297 of the ‘model truth’, prior to comparison with the reconstructions.

298 **3. Results**

299 *3.1 Performance metrics for the ‘SOCAT-baseline’ reconstruction*

300 The mean bias for the entire testbed period (i.e., 1982-2016) is 0.63 μatm globally (**Fig. 3a**) and
301 1.4 μatm for the Southern Ocean (< 35° S; **Table 1**). Bias is much closer to zero for the mid-

302 latitudes (between 35° S and 35° N; 0.23 μatm) and northern latitudes ($> 35^\circ$ N; 0.11 μatm) (**Fig.**
303 **3a**). There is a significant difference in bias considering southern hemisphere winter months (June,
304 July, August) versus summer months (December, January, February), with a global mean bias (for
305 1982-2016) of 1.3 μatm compared to 0.07 μatm , respectively (**Table 1**), due to the sparseness of
306 SOCAT observations from the southern hemisphere during the harsh winter season (**Fig. S5a**).
307 The mean RMSE for the entire testbed period (i.e., 1982-2016) is 11.8 μatm globally (**Fig. 3b**) and
308 11.5 μatm for the Southern Ocean (**Table 1**). RMSE is highest in the Eastern Tropical and
309 Southeastern Pacific Ocean and in the Southern Ocean, where the algorithm generally
310 overestimates pCO_2 (i.e., positive bias; **Fig. 3a**), with some exceptions in the Atlantic section. This
311 is consistent with the areas significantly undersampled by SOCAT (**Fig. S5b**). Except for these
312 areas, RMSE and bias is generally low (close to zero) in the open ocean, but show higher values
313 along coastlines (**Fig. 3b**).



314

315 **Figure 3:** Bias **(a)** and root-mean-squared error (RMSE) **(b)** for the ‘SOCAT-baseline’ (i.e., no USV) over the period
 316 of 1982 through 2016. The global mean bias and RMSE is 0.63 μatm and 11.8 μatm , respectively. Note that only the
 317 open ocean was considered in the reconstruction, so several areas were masked out prior to algorithm processing, such
 318 as the Arctic Ocean, coastal areas and marginal seas (no data; white areas in figures).

319

320

321 3.2 Reconstruction improvements with Saildrone USV additions

322 Our presentation of global maps is limited to runs ‘x5_5Y_W’ (5,022 monthly 1°x1° observations)
323 and ‘Z_x4_10Y_YR’ (7,600 monthly 1°x1° observations). These runs were selected as they
324 represent observational schemes that are realistic in the near-term future considering logistics and
325 cost level, both non-meridional and meridional sampling, and different approaches to observing
326 duration and seasonal coverage. For the remaining runs, equivalent maps can be found in the
327 **Supplement**.

328 3.2.1 Bias

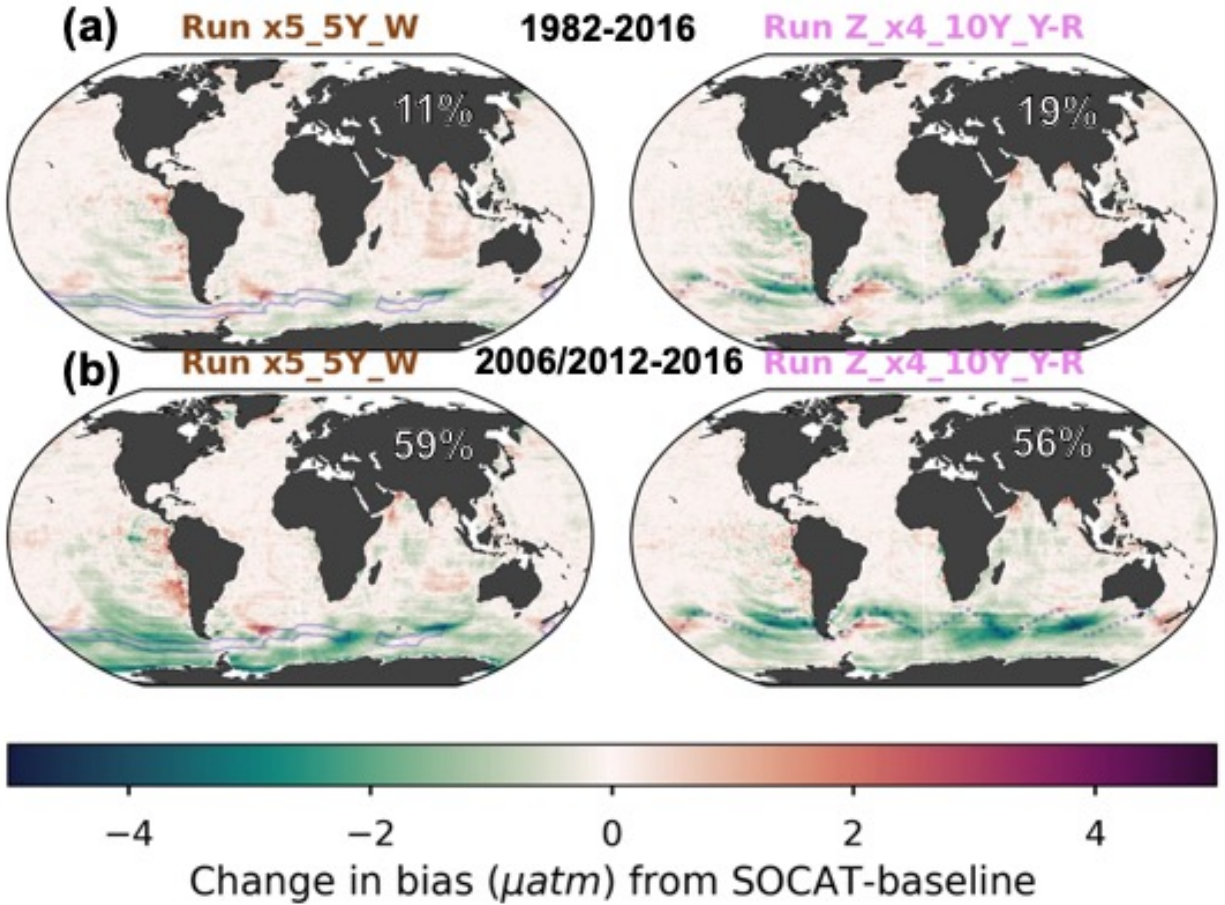
329 All Saildrone USV runs show a reduction in bias compared to the global mean 1982-2016
330 ‘SOCAT-baseline’ (**Figs. 4a, S6**). The improvement in bias is mainly due to lower reconstructed
331 pCO₂ values at southern latitudes, where the ‘SOCAT-baseline’ reconstruction generally
332 overestimates pCO₂ (**Fig. 3a**). The global mean bias for ‘zigzag’ run ‘Z_x4_10Y_YR’ is 0.51
333 µatm, a higher improvement (19 %) over the ‘SOCAT-baseline’ compared to the ‘one-latitude’
334 run ‘x5_5Y_W’ (11 % mean improvement; mean bias = 0.57 µatm;) (**Fig. 4a; Table 1**). Generally,
335 the ‘zigzag’ runs show higher improvements from the ‘SOCAT-baseline’ (19-31 % improvement;
336 resulting mean bias = 0.44-0.51 µatm) compared to the ‘one-latitude’ runs (7-19 % improvement;
337 resulting mean bias = 0.52-0.59 µatm) (**Fig. S6; Table 1**). However, the ‘one-latitude’-run
338 ‘x13_10Y_W’ that samples southern hemisphere winter months only, stands out with the lowest
339 global mean bias of 0.39 µatm, representing a 39 % mean improvement from the ‘SOCAT-
340 baseline’, as well as reduced spread across the 75 ensemble members (**Table 1; Fig. S6, S7, S8**).
341 This run, however, has three or five times more observations (25,395) than ‘Z_x4_10Y_YR’ and
342 ‘x5_5Y_W’, respectively.

343 Compared to the entire testbed period, even larger improvements in global mean bias are
344 shown for the period of Saildrone USV additions (2006-2016 and 2012-2016; **Figs. 4a vs. 4b,**
345 **Figs. S6 vs. S7**). Compared to the ‘SOCAT-baseline’, run ‘x13_10Y_W’ results in a mean bias
346 improvement of 95 %, while the remaining ‘one-latitude’ runs and the ‘zigzag’ runs show mean
347 improvements up to 63 % and 85 %, respectively (**Fig. S7**).

348 Perhaps surprisingly, there is not a strong connection between the global or Southern Ocean
349 mean bias and the number of added USV observations (**Fig. 5**). The ‘one-latitude’ ‘high-sampling’

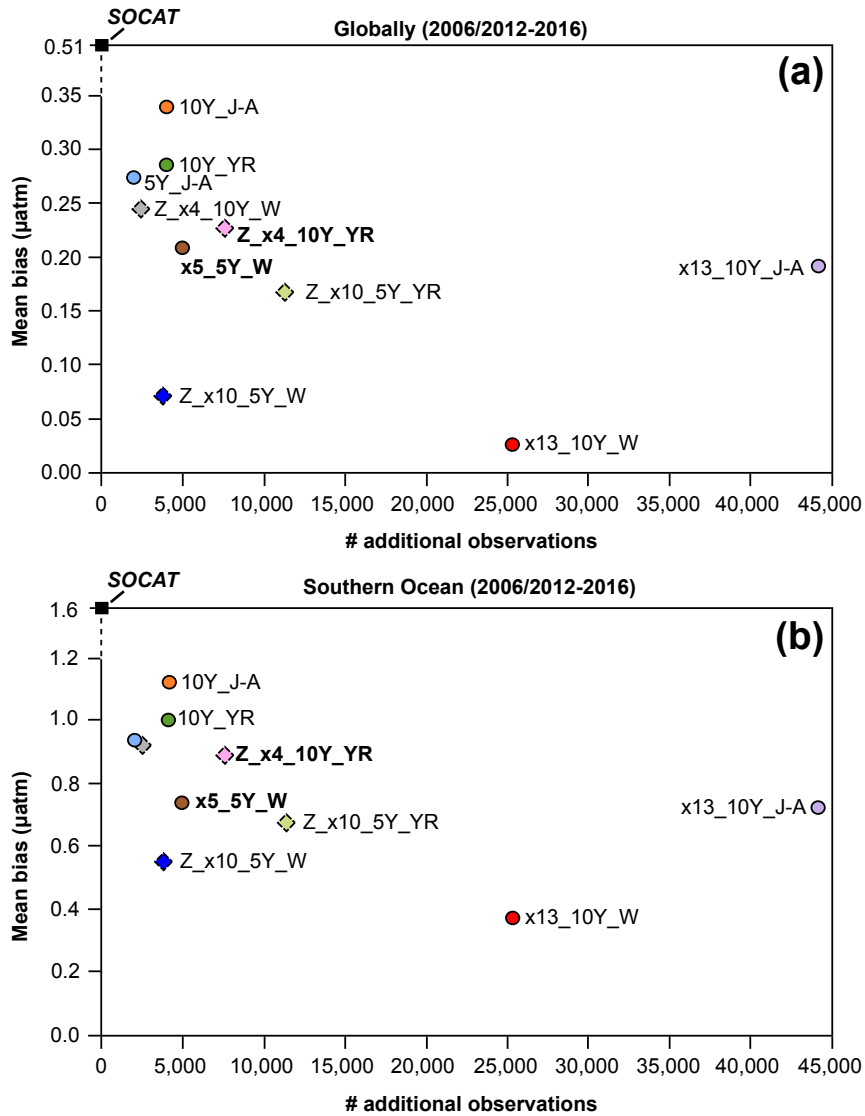
350 run ‘x13_10Y_J-A’ (44,250 observations) show similar mean bias or is outperformed by all
351 ‘zigzag’ runs as well as the ‘one-latitude’-runs that restrict sampling to southern hemisphere winter
352 months (i.e., ‘x5_5Y_W’ and ‘x13_10Y_W’).

353 Considering the change in bias from year-to-year, the ‘SOCAT-baseline’ shows positive
354 bias at all latitudes in the beginning of the testbed period, before improvement occurs around 1990
355 (**Fig. 6a**). This is consistent with increasing SOCAT sampling with time for the period considered
356 here (i.e., up to 2016; **Fig. S5c**). As SOCAT observations are biased towards the northern
357 hemisphere (**Fig. S5a, b**), bias in the Southern Ocean ($< 35^\circ$ S) increases significantly starting in
358 the 2000s and remains high until the end of the testbed period (**Fig. 6a**). By adding USV sampling,
359 bias in the Southern Ocean improves over the ‘SOCAT-baseline’ around year 2000 (**Fig. 6b-d**;
360 **Fig. S9**), up to 6-12 years before to the introduction of additional samples in either 2006 or 2012.
361 This improvement is shown for the majority of the 75 ensemble members (**Fig. S10**). Run
362 ‘Z_x10_5Y_W’, which has the lowest mean bias out of the ‘zigzag’ runs (**Fig. 5**), shows
363 improvement even further back in time, until the beginning of the testbed period (**Fig. S9**). While
364 the annual mean bias of the ‘zigzag’ runs varies rather consistently, there is a larger spread across
365 the ‘one-latitude’ runs (**Fig. 6d**).

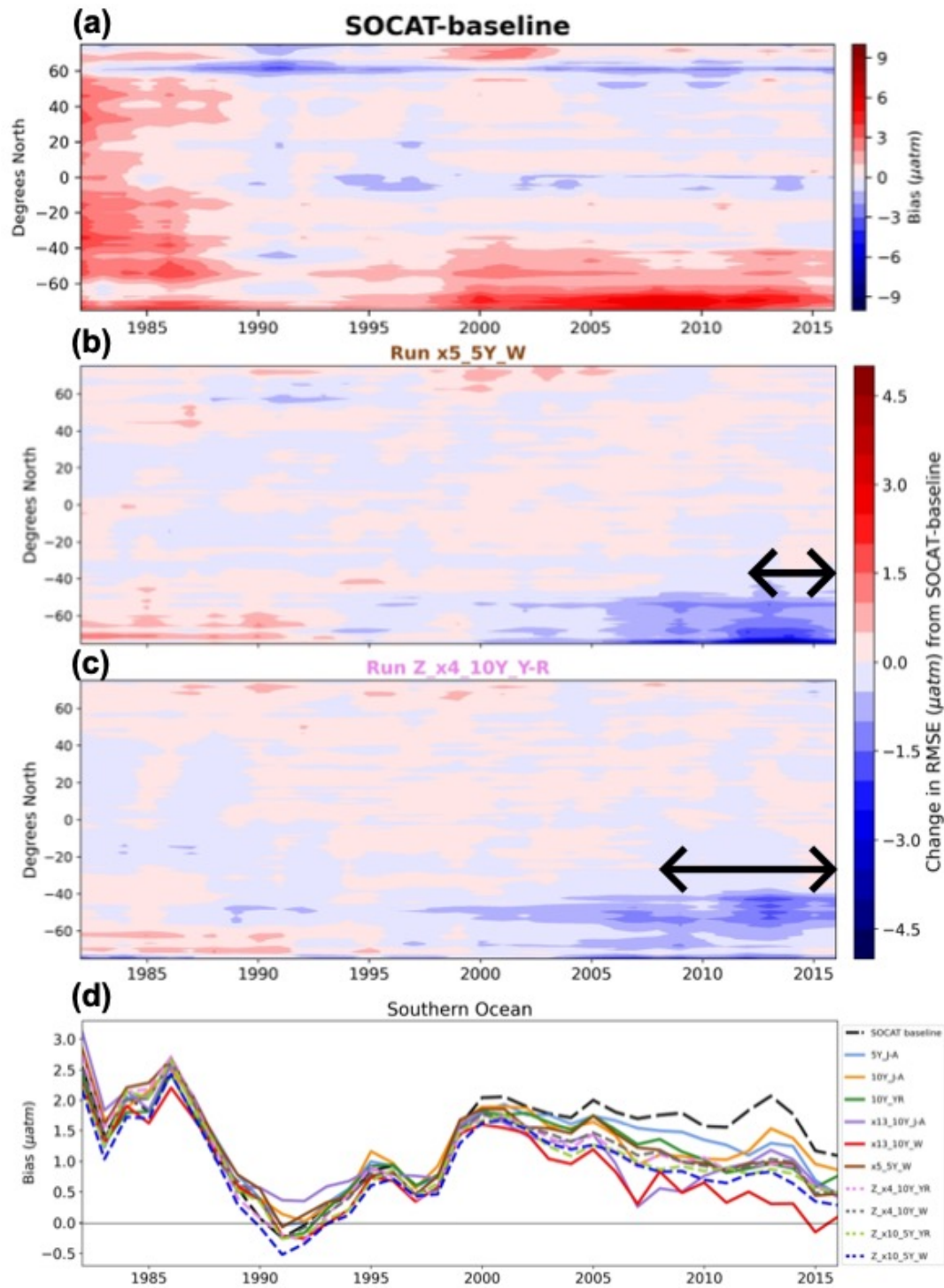


366
 367
 368
 369
 370

Figure 4: Change in bias when comparing run ‘x5_5Y_W’ and ‘Z_x4_10Y_YR’ to the ‘SOCAT-baseline’ reconstruction, averaged over the duration of the testbed period (a; 1982-2016) and the period of USV additions (b; 2006-2012 or 2012-2016). The percent global improvement in absolute bias is shown on each panel.



371
 372 **Figure 5:** Mean bias globally (a) and for the Southern Ocean (b) for the duration of Saildrone USV sampling (2006-
 373 2016 or 2012-2016) for all runs presented in **Table 1**. Circles represent runs using the ‘one-latitude’ track, while
 374 diamonds represent ‘zigzag’ runs. Runs highlighted in bold correspond to the two selected runs mapped in **Figure 4**,
 375 **6**, **7** and **9**. Global (0.51 µatm) and Southern Ocean (1.6 µatm) bias values shown for the ‘SOCAT-baseline’ (black
 376 squares) represent a mean of values for 2006-2016 (global = 0.52 µatm, S. Ocean = 1.63 µatm) and 2012-2016 (global
 377 = 0.51 µatm, S. Ocean = 1.56 µatm). ‘# additional observations’ = number of monthly 1°x1° USV observations in
 378 addition to SOCAT. Box plots illustrating the spread across the 75 ensemble members are shown in **Fig. S8**.



380

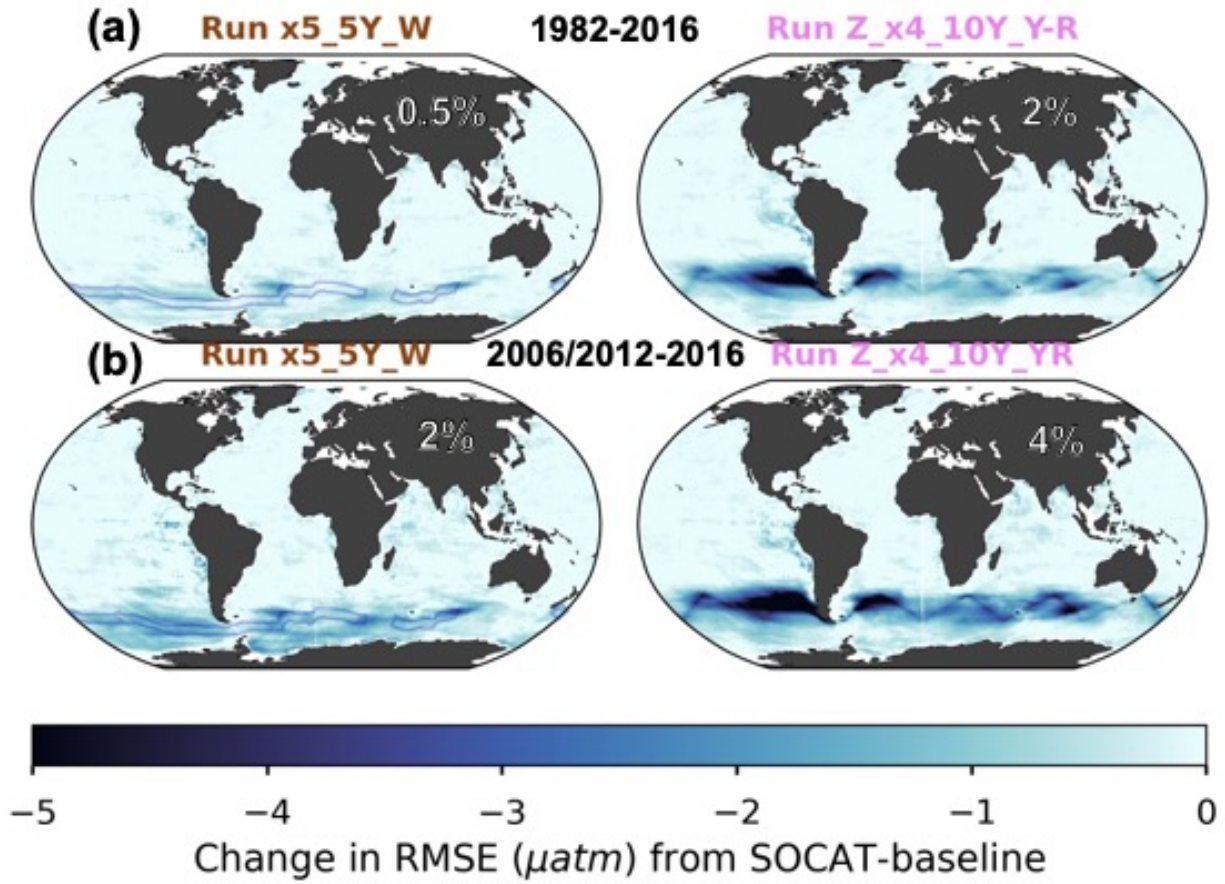
381 **Figure 6:** Zonal mean, annual mean Hovmöller of bias for the 'SOCAT-baseline' (a). Change in bias for run
 382 'x5_5Y_W' (b) and 'Z_x4_10Y_YR' (c) compared to the 'SOCAT-baseline' shown in (a). Improvement in bias in
 383 the Southern Ocean expands back in time well beyond the duration of USV additions for both runs (shown by arrows
 384 on each panel). Annual mean bias for the Southern Ocean (> 35° S) for all runs (d).

385

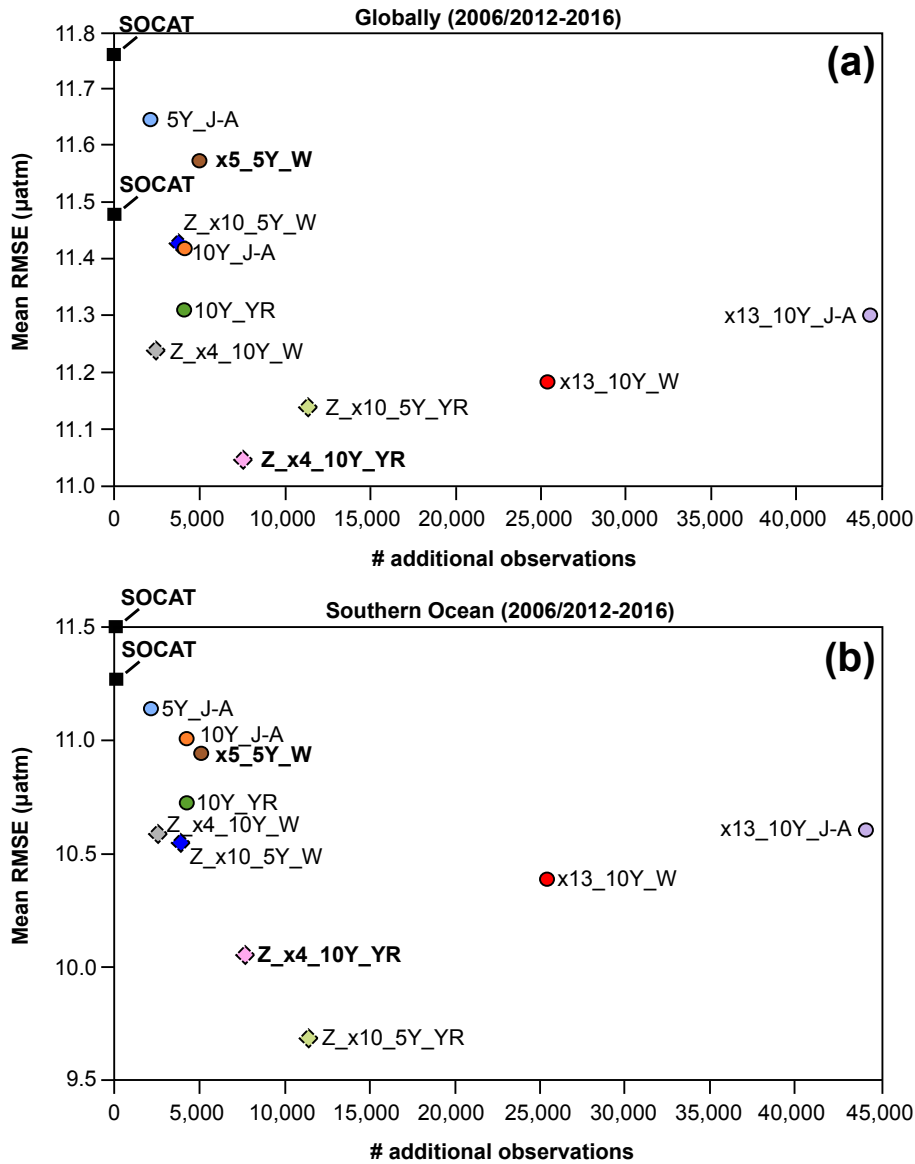
386 3.2.2 Root-mean squared error (RMSE)

387 Similar to bias, improvements in RMSE are most significant during the period of USV additions
388 and within the Southern Ocean (**Fig. 7a** vs. **7b**). For the duration of USV additions, the ‘one-
389 latitude’ runs show improvements in global mean RMSE of 1-3 % (0.1-1 % for 1982-2016), while
390 the ‘zigzag’ runs show higher improvements between 2-5 % (1-3 % for 1982-2016) (**Figs. 7, S11,**
391 **S12**). Mean RMSE is further reduced in the Southern Ocean by up to 16 %, and during southern
392 hemisphere winter months (JJA) up to 21 % (run ‘Z_x10_5Y_YR’; mean RMSE of 9.6 μatm ;
393 **Table 1**). There is minimal change in RMSE (or bias) during southern hemisphere summer months
394 (DJF; **Fig. S13**). The two ‘zigzag’ runs sampling year-round (‘Z_x4_10Y_YR’ and
395 ‘Z_x10_5Y_YR’) have the lowest RMSE values both globally and in the Southern Ocean (**Fig. 8**).
396 The spread across the 75 testbed members for each experiment is shown in **Figure S14**.

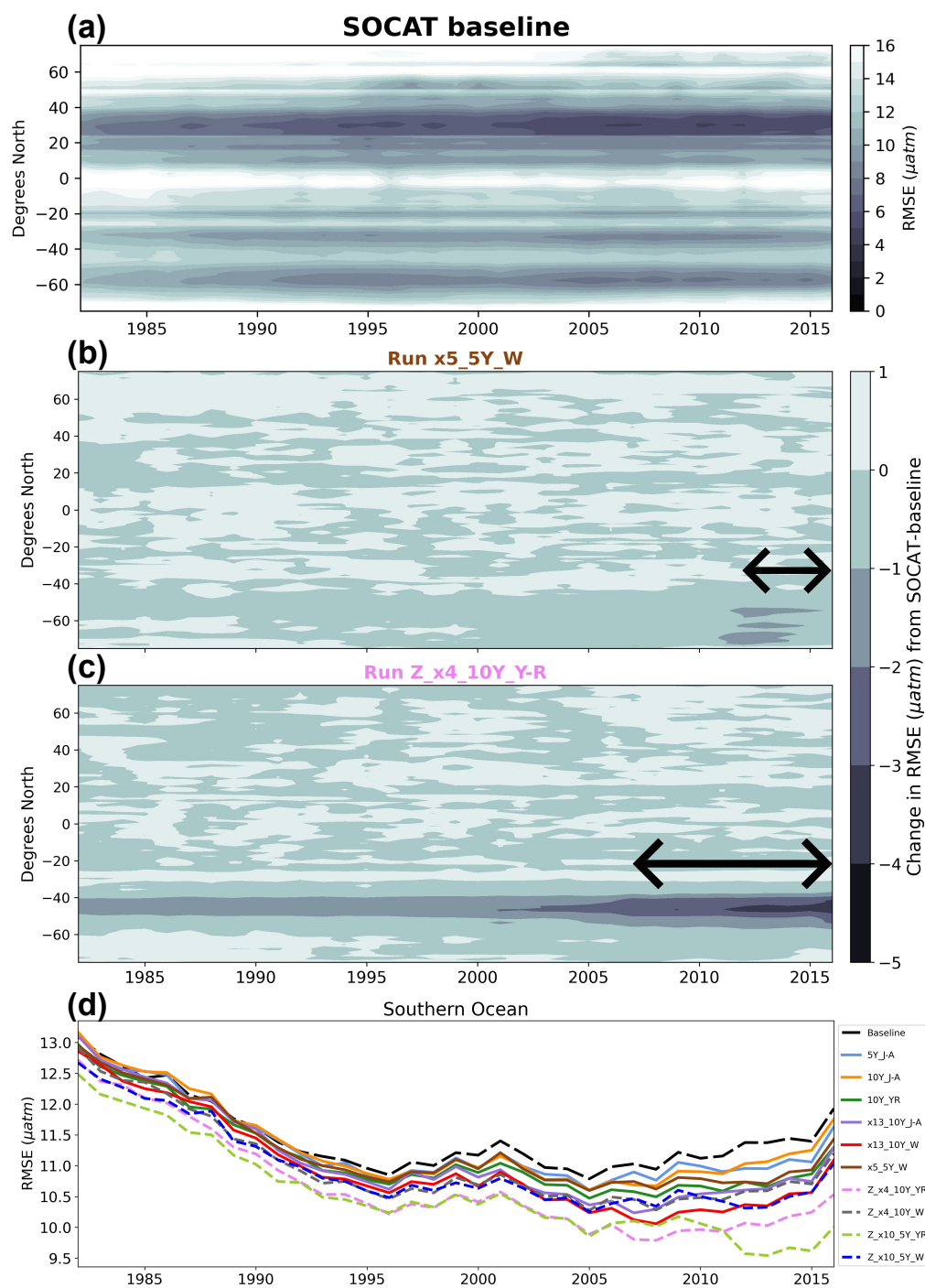
397 The ‘zigzag’ runs, as well as the ‘high-sampling’ ‘one-latitude’-runs (i.e., ‘x13_10Y_J-A’
398 and ‘x13_10Y_W’), show improvements compared to the ‘SOCAT-baseline’ from the initiation
399 of sampling (**Figs. 9, S15, S16**). The year-round ‘zigzag’ runs, however, show improvement in the
400 Southern Ocean from the beginning of the testbed period (**Figs. 9c, d, S15**). RMSE improvements
401 back in time are greater for all runs in the southern hemisphere winter months (**Fig. S17**).



402
 403 **Figure 7:** Change in RMSE when comparing run 'x5_5Y_W' and 'Z_x4_10Y_YR' to the 'SOCAT-baseline',
 404 averaged over the duration of the testbed period (**a**; 1982-2016) and the period of Saildrone USV additions (**b**; 2006-
 405 2012 or 2012-2016). The percent global improvement is shown on each panel.



406
 407 **Figure 8:** Mean RMSE globally (a) and for the Southern Ocean (< 35° S; b) for the duration of Sairdron USV
 408 sampling (2006-2016 or 2012-2016) for all runs presented in **Table 1**. Circles represent runs using the ‘one-latitude’
 409 track, while diamonds represent ‘zigzag’ runs. Runs highlighted in bold correspond to the two selected runs mapped
 410 in **Figure 4, 6, 7 and 9**. RMSE values shown for the ‘SOCAT-baseline’ (black squares) represent a mean of values
 411 for 2006-2016 (global = 11.5 µatm, S. Ocean = 11.3 µatm) and 2012-2016 (global = 11.8 µatm, S. Ocean = 11.5 µatm).
 412 ‘# additional observations’ = number of monthly 1°x1° USV observations in addition to SOCAT. Box plots illustrating
 413 the spread across the 75 ensemble members are shown in **Fig. S14**.



415

416 **Figure 9:** Zonal mean, annual mean Hovmöller of RMSE for the ‘SOCAT-baseline’ (a). Change in RMSE for run
 417 ‘x5_5Y_W’ (b) and ‘Z_x4_10Y_YR’(c) compared to the ‘SOCAT-baseline’. Run ‘Z_x4_10Y_YR’ shows
 418 improvement in RMSE within the Southern Ocean, which expand well beyond the duration of Saildrone USV
 419 additions (shown by arrow on panel). Annual mean RMSE for the Southern Ocean (> 35° S) for all runs (d).

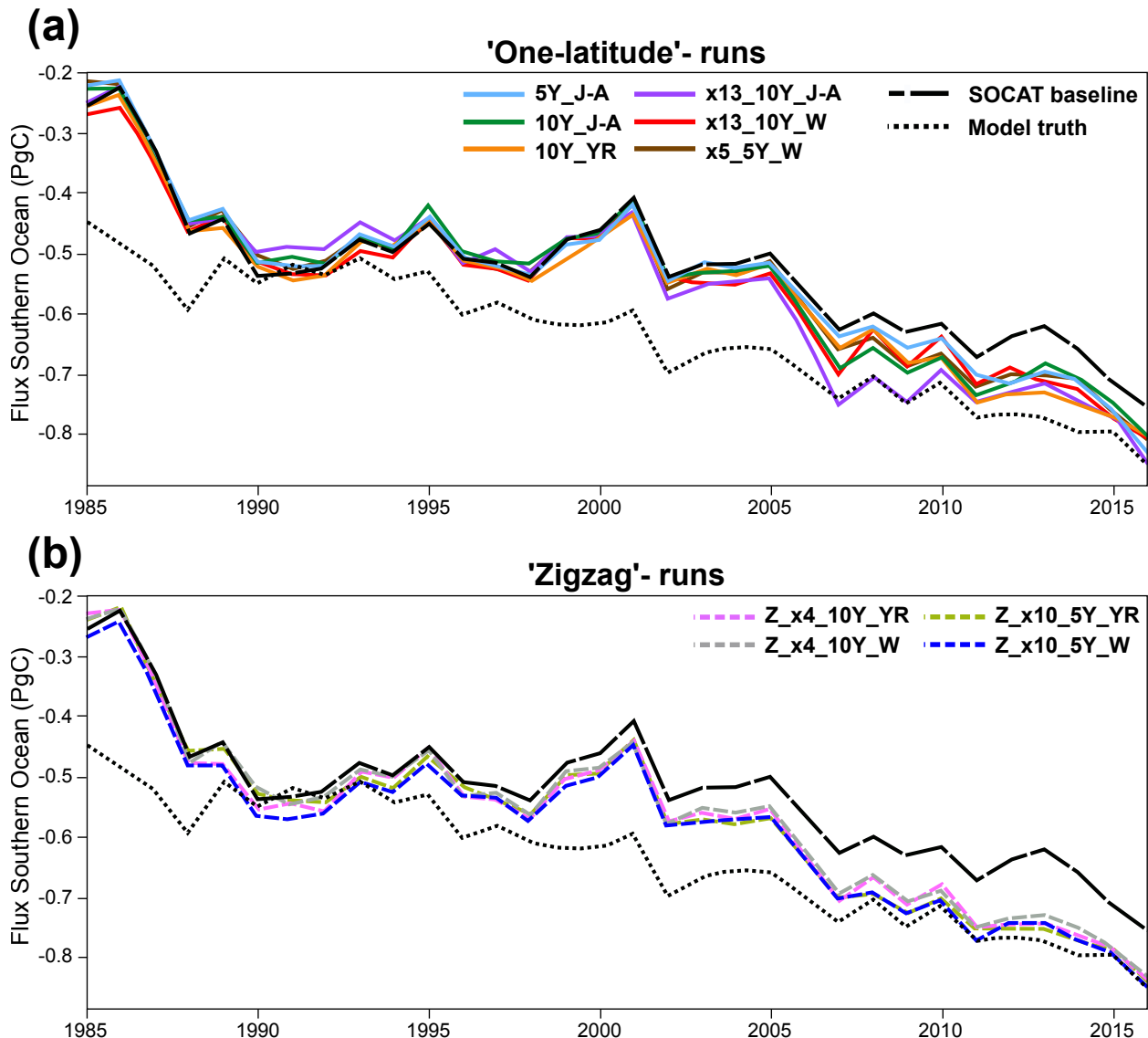
420

421 *3.3 Impact on the air-sea CO₂ flux with Saildrone USV additions*

422 Air-sea flux was calculated in the same manner for both the ML reconstructions and the ‘model
423 truth’, which allows for the isolation of the impact of different sampling strategies, as mediated by
424 the pCO₂ reconstruction, on fluxes (see **Sect. 2.5**). These flux estimates are made to inform
425 understanding of the errors that may exist in CO₂ flux estimates derived from pCO₂
426 reconstructions, and how new sampling could address these errors. Flux estimates represent the
427 average of the 75 members of the LET in each case, and are not estimates of real-world fluxes.

428 Compared to the ‘model truth’, the ‘SOCAT-baseline’ reconstruction underestimates the
429 global and Southern Ocean sink by 0.11-0.13 Pg C yr⁻¹ over 1982-2016 (**Fig. 10; Table S1**).
430 Regardless of sampling pattern, adding Saildrone USV observations increases both the global and
431 Southern Ocean mean sink compared to the ‘SOCAT-baseline’ (**Figs. 10, S18**). The ‘one-latitude’
432 runs show an increase of 0.01-0.03 Pg C yr⁻¹ (2-6 % strengthening) of the Southern Ocean sink
433 (1982-2016), while the ‘zigzag’ runs lead to an even stronger sink by 0.04-0.06 Pg C yr⁻¹ (7-11 %
434 strengthening) (**Table S2**). When averaging over the years of Saildrone USV sampling addition
435 (i.e., 2006-2012 and 2012-2016), the Southern Ocean sink increases up to 0.09 Pg C yr⁻¹ (14 %
436 strengthening) for the ‘one-latitude’ runs and up to 0.1 Pg C yr⁻¹ (15 % strengthening) for the
437 ‘zigzag’ runs (**Table S2**). These same features are found for the global ocean (**Fig. S18; Table**
438 **S2**).

439 All of the ‘zigzag’ runs quite closely match both the global and Southern Ocean ‘model
440 truth’ air-sea CO₂ flux for the duration of sample additions (**Figs. 10, S18**). Except for the first
441 couple of years of sample addition for the ‘high-sampling’-run ‘x13_10Y_J-A’, none of the ‘one-
442 latitude’ runs can match the ‘model truth’ air-sea CO₂ flux, instead they all underestimate the flux
443 (**Figs. 10, S18**). The ‘zigzag’ runs have impact on the air-sea flux from an earlier date, starting to
444 pull the results away from the ‘SOCAT-baseline’ and toward the ‘model truth’ already in the late-
445 1990s, while the ‘one-latitude’ runs do the same about a decade later (**Figs. 10, S18**).



446 **Figure 10:** Southern Ocean (< 35° S) annually averaged air-sea CO₂ flux for the ‘SOCAT-baseline’ (black dashed
 447 line), ‘model truth’ (black dotted line) ‘one-latitude’ runs (a; solid lines) and ‘zigzag’ runs (b; dashed lines).
 448

449

450

451 **4. Discussion**

452 We have tested the pCO₂-Residual reconstruction method with the Large Ensemble Testbed (LET)
 453 to estimate its fidelity and understand how new samples could increase skill. We find that,
 454 regardless of the chosen Sairdrone USV sampling pattern, the reduction in mean bias and mean
 455 RMSE compared to the ‘SOCAT-baseline’ is most prominent within the Southern Ocean (< 35°
 456 S) during the period of which Sairdrone USV observations were added (Figs. 4, 6, 7, 9). However,
 457 it is important to mention that additional Southern Ocean sampling also improves pCO₂

458 reconstructions globally (**Figs. 5a, 8a**). Based on our experiments, a combination of factors
459 improve global and Southern Ocean pCO₂ reconstructions, including the type of sampling pattern
460 and seasonality of sampling, and to some extent, the number of additional observations.
461 Importantly, increasing the number of observations or duration of sampling (5 vs. 10 years) is not
462 the sole determining factor for improving the reconstructions (**Figs. 5, 8**). This is best demonstrated
463 by the ‘high-sampling’-run ‘x13_10Y_J-A’ (44,250 observations), which does not provide
464 significantly better reconstructions, or is even outperformed, by runs with 2-18 times fewer
465 observations. The runs that produce lower mean RMSE do include data throughout southern
466 hemisphere winter (**Figs. 8, 9d**). Run ‘x13_10Y_J-A’ does not include more than a few
467 observations in the month of August, as it follows the temporal pattern of the real-world ‘one-
468 latitude’ Saildrone USV expedition (**Fig. S2**; Sutton et al., 2021). The ‘one-latitude’ runs ‘10Y_J-
469 A’ and ‘10Y_YR’ are directly comparable in terms of sample duration, spatial extent and number
470 of observations (**Table 1**), but the latter, which covers all months, always shows lower mean
471 RMSE and bias (**Figs. 5, 6d, 8, 9d**). These examples attest to the importance of addressing the
472 issue of significant undersampling in the Southern Ocean during the winter season (**Figs. S5a, b**).

473 Another important comparison is the ‘one-latitude’-run ‘x5_5Y_W’ (5,022 observations)
474 and ‘zigzag’-run ‘Z_x10_5Y_W’ (3,800 observations) that both sample during southern
475 hemisphere winter months over a five-year period (**Table 1**), where the ‘zigzag’-run consistently
476 performs better even though it includes fewer observations (**Figs. 5, 8**). Most of the runs that
477 perform similar to, or outperform, the above-mentioned ‘high-sampling’-run ‘x13_10Y_J-A’
478 (44,250 observations), sample in a ‘zigzag’ pattern. Out of all 10 runs, the ‘year-round’ ‘zigzag’
479 runs (‘Z_x4_10Y_YR’ and ‘Z_x10_5Y_YR’) are most able to reduce the mean error as shown by
480 the lowest RMSE values (**Figs. 8, 9d**). A recent study performed similar sampling experiments as
481 shown here, by comparing sampling from different types of autonomous platforms to a ‘SOCAT-
482 baseline’ (Djeutchouang et al., 2022). They emphasized the importance of capturing the significant
483 differences in pCO₂ that exist across meridional gradients during summer and winter months (up
484 to 15 µatm; Djeutchouang et al., 2022). The meridional coverage provided by the ‘zigzag’ runs
485 could explain why these runs generally outperform the ‘one-latitude’ runs in our study, and show
486 significant reduction in both RMSE and bias, even though the global pCO₂ data density is raised
487 by as little as 0.01-0.07 %.

488 The greatest reduction of mean bias out of all runs is shown by run ‘x13_10Y_W’ (**Figs.**
489 **5, 6d**), which represents ‘one-latitude’ ‘high-sampling’ (i.e., 25,395 observations) during southern
490 hemisphere winter months only. This sampling strategy seems thus to have a higher ability to
491 reduce the ML model’s tendency to overestimate pCO₂ in the Southern Ocean compared to any of
492 the meridional (‘zigzag’) runs. However, it should be noted that run ‘x13_10Y_W’ covers areas
493 south of 55° S (**Fig. S4**), and its improvement in mean bias (and mean RMSE) is particularly
494 prevalent at these high latitudes (e.g., **Figs. S7, S9, S12, S17**). Whether or not this run is, in fact,
495 feasible with current or future technology is uncertain as parts of the southernmost tracks
496 potentially cover the Southern Ocean ice zone (**Fig. S19**), and solar radiation for solar-powered
497 platforms and sensors becomes very limited during winter south of 55° S. Furthermore, this
498 particular sampling strategy requires 13 USVs, and so would be the most costly of the observing
499 scenarios. Although run ‘x13_10Y_W’ demonstrates the highest reduction in mean bias out of all
500 runs, the ‘zigzag’ runs still reduce mean bias in the Southern Ocean by 44-65 % (vs. 77 % for run
501 ‘x13_10Y_W’).

502 Overall, the ‘zigzag’ runs include significantly fewer observations, require fewer USVs,
503 collect samples over the same duration, or even half the time as run ‘x13_10Y_W’, cover areas
504 north of 55°S and within the ice-free zone, and show major improvement in the reconstruction of
505 pCO₂, attested to by reductions in both bias and RMSE. The ‘zigzag’ runs also closely match both
506 the global and Southern Ocean ‘model truth’ air-sea CO₂ flux for the duration of sample additions
507 (**Figs. 10, S18**). It also appears that the ‘zigzag’ runs generally have a greater impact on both the
508 pCO₂ reconstruction and the air-sea flux further back in time, starting to deviate from the ‘SOCAT-
509 baseline’ earlier compared to the ‘one-latitude’ runs (**Figs. 6, 9, 10, S9, S15, S17, S18**). Even the
510 ‘zigzag’ scenarios with the least number of USVs (e.g., ‘Z_x4_10Y_YR’) reduces Southern Ocean
511 reconstruction bias and RMSE by up to 46 % and 11 %, respectively, and could provide a basis
512 for realistic future Southern Ocean pCO₂ sampling campaigns.

513 The main motivation for improving surface ocean pCO₂ reconstructions is so that we can
514 more accurately estimate the current and future oceanic uptake of anthropogenic carbon. The
515 Southern Ocean is a significant carbon sink, but estimates of the air-sea CO₂ flux diverge
516 substantially in this region (Takahashi et al., 2009; Landschützer et al., 2014, 2015; Rödenbeck et
517 al., 2015; Williams et al., 2017; Gray et al., 2018; Gruber et al., 2019; Bushinsky et al., 2019; Long

518 et al., 2021; Fay and McKinley, 2021; Wu et al., 2022). Southern Ocean estimates incorporating
519 observations from biogeochemical floats have shown a significantly weaker sink compared to
520 those based only on observations from ships (Williams et al., 2017; Gray et al., 2018; Bushinsky
521 et al., 2019). Bushinsky et al. (2019) and Hauck et al. (2023) performed similar sampling
522 experiments as presented here, by comparing ML surface ocean pCO₂ reconstructions based on
523 SOCAT vs. additional SOCCOM or ideal virtual floats. These studies showed that SOCAT
524 sampling alone overestimates the CO₂ uptake in the Southern Ocean, and that additional floats
525 reduce this overestimation, leading to a decreased (weakened) ocean carbon sink. In contrast, we
526 find that the pCO₂-Residual method underestimates the CO₂ uptake with only SOCAT sampling,
527 and that adding USVs increased (strengthened) the Southern Ocean and global ocean sink by up
528 to 0.1 Pg C yr⁻¹ (**Figs. 10, S18; Table S2**).

529 Going forward, additional studies are needed to better understand why these results suggest
530 a different direction of the sink change with additional sampling. These differences could stem
531 from the use of different reconstruction methods assessed. Hauck et al. (2023) used the MPI-SOM-
532 FFN and CarboScope/Jena-MLS reconstruction methods, while we use the pCO₂-Residual
533 method. Another substantial difference between the studies is the models and numbers of ensemble
534 members used as the testbed. Hauck et al. (2023) use a single hindcast model, while we use 25
535 members each from three Earth System Models. We find substantial spread across these 75
536 members (**Figs. S8, S10, S14, S16**), indicating that model structure and internal variability
537 significantly impact results. Our study and Hauck et al. (2023) use different approaches for the
538 calculation of fluxes, which could also be a factor. Targeted, coordinated studies using multiple
539 reconstruction approaches with consistent testbed structures and experimental approaches are
540 clearly needed (Rödenbeck et al., 2015). Despite this need for this additional work, studies do
541 agree that additional Southern Ocean observations could significantly improve reconstructions of
542 air-sea CO₂ fluxes.

543 What else can we learn using the model testbed? The ‘SOCAT-baseline’ demonstrates a
544 weakening of the global and Southern Ocean carbon sink starting in the 1990s with a peak around
545 year 2000 (**Figs. 10, S18**), which is in broad agreement with various data products using real-world
546 SOCAT data (e.g., Gruber et al., 2019; Landschützer et al., 2015; Bushinsky et al., 2019;
547 Bennington et al., 2022; Gloege et al., 2022). Peaks in bias and RMSE coincide in time with the

548 weakening sink (**Figs. 6d, 9d**). As shown by **Figure 10**, this ‘low sink’ is significantly exaggerated
549 compared to the ‘model truth’. To better understand this discrepancy, we performed an additional
550 experiment based on run ‘Z_x10_5Y_YR’, but assumed sampling every year for the entire testbed
551 period (i.e., 1982-2016). There is now a significant reduction in the temporal variability of
552 reconstruction bias; with the additional 35-year USV sampling, the reconstructed Southern Ocean
553 air-sea CO₂ flux closely matches the ‘model truth’ for the entire testbed duration (**Fig. S20**). This
554 suggests that the large decadal variability of air-sea CO₂ fluxes since the 1980s, and the weak
555 anomaly in the Southern Ocean carbon sink in the early 2000s (Le Quéré et al., 2007; Landschützer
556 et al., 2015; Gruber et al., 2019; Bennington et al., 2022a,b; Friedlingstein et al., 2023), may be at
557 least partially attributable to undersampling of the Southern Ocean. This is in agreement with the
558 float sampling experiments performed by Hauck et al. (2023), attributing the strong decadal
559 variability to sparse and skewed SOCAT data distributions. We will further explore this issue in
560 future work. Still, this preliminary experiment suggests that interpretations of trends and variability
561 of the global and Southern Ocean carbon sink should be considered with caution.

562 **5. Conclusions**

563 By using the Large Ensemble Testbed (LET), we show that targeted meridional and winter
564 sampling in the Southern Ocean can improve global and Southern Ocean ML surface ocean pCO₂
565 reconstructions. Significant improvements are possible by raising the global pCO₂ data density by
566 as little as 0.01-0.07 %. Further, we find that this modest amount of additional Saildrone USV
567 sampling increases the global and Southern Ocean air-sea CO₂ flux by up to 0.1 Pg C yr⁻¹, a
568 quantity equivalent to 25 % of the uncertainty in the ocean carbon sink (0.4 Pg C yr⁻¹;
569 Friedlingstein et al., 2023). Our findings are consistent with previous studies suggesting that
570 additional observations during southern hemisphere winter months and covering meridional
571 gradients can reduce uncertainties and biases in the reconstructions (Lenton et al., 2006; Monteiro
572 et al., 2010; Djeutchouang et al., 2022; Mackay et al., 2022). As opposed to other autonomous
573 platform approaches, Saildrone USVs obtain in situ pCO₂ observations with uncertainties
574 equivalent to the highest-quality observations collected by research ships ($\pm 2 \mu\text{atm}$; Sabine et al.,
575 2020; Sutton et al., 2021), and can operate at a high speed so that the spatial extent and seasonal
576 cycle of meridional gradients can be covered. The approach of combining high-accuracy Saildrone
577 USV and SOCAT observations represents thus a promising solution to improve future surface

578 ocean pCO₂ reconstructions and the accuracy of the ocean carbon sink. Lastly, we show that the
579 large variability in bias, and the weakening of the global and Southern Ocean carbon sink in the
580 2000s, may be partially an artefact of Southern Ocean undersampling.

581 **Code availability**

582 Data analysis scripts will be made available in a GitHub repository upon publication.

583 **Data availability**

584 The Large Ensemble Testbed is publicly available at
585 https://figshare.com/collections/Large_ensemble_pCO2_testbed/4568555.

586

587 **Author contribution**

588 THH, GAM and AJS designed the experiments, and THH performed the simulations. THH, ARF
589 and LG developed the code. THH and ARF calculated the air-sea fluxes. THH prepared the
590 manuscript with contributions from all co-authors.

591 **Competing interests**

592 The authors declare that they have no conflict of interest.

593 **Acknowledgements**

594 We acknowledge funding from NOAA through the Climate Observations and Monitoring Program
595 (Award #NA20OAR4310340) and from NSF through the LEAP STC (Award #2019625). This is
596 PMEL contribution 5549. We would also like to acknowledge and thank Val Bennington, Julius
597 Busecke, Devan Samant and Abby Shaum for providing technical support.

598

599 **References**

600

601 Bakker, D. C. E., Pfeil, B., Landa, C. S., Metzl, N., O'Brien, K. M., Olsen, A., Smith, K., Cosca,
602 C., Harasawa, S., Jones, S. D., Nakaoka, S., Nojiri, Y., Schuster, U., Steinhoff, T., Sweeney, C.,

603 Takahashi, T., Tilbrook, B., Wada, C., Wanninkhof, R., Alin, S. R., Balestrini, C. F., Barbero, L.,
604 Bates, N. R., Bianchi, A. A., Bonou, F., Boutin, J., Bozec, Y., Burger, E. F., Cai, W.-J., Castle, R.
605 D., Chen, L., Chierici, M., Currie, K., Evans, W., Featherstone, C., Feely, R. A., Fransson, A.,
606 Goyet, C., Greenwood, N., Gregor, L., Hankin, S., Hardman-Mountford, N. J., Harlay, J., Hauck,
607 J., Hoppema, M., Humphreys, M. P., Hunt, C. W., Huss, B., Ibánhez, J. S. P., Johannessen, T.,
608 Keeling, R., Kitidis, V., Körtzinger, A., Kozyr, A., Krasakopoulou, E., Kuwata, A., Landschützer,
609 P., Lauvset, S. K., Lefèvre, N., Lo Monaco, C., Manke, A., Mathis, J. T., Merlivat, L., Millero, F.
610 J., Monteiro, P. M. S., Munro, D. R., Murata, A., Newberger, T., Omar, A. M., Ono, T., Paterson,
611 K., Pearce, D., Pierrot, D., Robbins, L. L., Saito, S., Salisbury, J., Schlitzer, R., Schneider, B.,
612 Schweitzer, R., Sieger, R., Skjelvan, I., Sullivan, K. F., Sutherland, S. C., Sutton, A. J., Tadokoro,
613 K., Telszewski, M., Tuma, M., van Heuven, S. M. A. C., Vandemark, D., Ward, B., Watson, A.
614 J., and Xu, S.: A multi-decade record of high-quality $f\text{CO}_2$ data in version 3 of the Surface Ocean
615 CO_2 Atlas (SOCAT), *Earth System Science Data*, 8, 383–413, [https://doi.org/10.5194/essd-8-383-](https://doi.org/10.5194/essd-8-383-2016)
616 [2016](https://doi.org/10.5194/essd-8-383-2016), 2016.

617 Bakker, D. C. E., Alin, S. R., Becker, M., Bittig, H. C., Castaño-Primo, R., Feely, R. A., Gkritzalis,
618 T., Kadono, K., Kozyr, A., Lauvset, S. K., Metzl, N., Munro, D. R., Nakaoka, S., Nojiri, Y., O'Brien,
619 K. M., Olsen, A., Pfeil, Benjamin, P., Denis, S., Tobias, S., Kevin F., Sutton, A. J., Sweeney, C.,
620 Tilbrook, B., Wada, C., Wanninkhof, R., Willstrand W. A., Akl, J., Apelthun, L. B., Bates, N.,
621 Beatty, C. M., Burger, E. F., Cai, W., Cosca, C. E., Corredor, J. E., Cronin, M., Cross, J. N., De
622 Carlo, E. H., DeGrandpre, M. D., Emerson, S. R., Enright, M. P., Enyo, K., Evans, W., Frangoulis,
623 C., Fransson, A., García-Ibáñez, M. I., Gehrung, M., Giannoudi, L., Glockzin, M., Hales, B.,
624 Howden, S. D., Hunt, C. W., Ibánhez, J. S. P., Jones, S. D., Kamb, L., Körtzinger, A., Landa, C.
625 S., Landschützer, P., Lefèvre, N., Lo Monaco, C., Macovei, V. A., Maenner J. S., Meinig, C.,
626 Millero, F. J., Monacci, N. M., Mordy, C., Morell, J. M., Murata, A., Musielewicz, S., Neill, .,
627 Newberger, T., Nomura, D., Ohman, M., Ono, T., Passmore, A., Petersen, W., Petihakis, G.,
628 Perivoliotis, L., Plueddemann, A. J., Rehder, G., Reynaud, T., Rodriguez, C., Ross, A. C.,
629 Rutgersson, A., Sabine, C. L., Salisbury, J. E., Schlitzer, R., Send, U., Skjelvan, I., Stamatakis, N.,
630 Sutherland, S. C., Sweeney, C., Tadokoro, K., Tanhua, T., Telszewski, M., Trull, T., Vandemark,
631 D., van Ooijen, E., Voynova, Y. G., Wang, H., Weller, R. A., Whitehead, C., Wilson, D.: Surface
632 Ocean CO_2 Atlas Database Version 2022 (SOCATv2022) (NCEI Accession 0253659), NOAA

633 National Centers for Environmental Information [dataset], <https://doi.org/10.25921/1h9f-nb73>,
634 2022.

635 Bennington, V., Galjanic, T., and McKinley, G. A.: Explicit Physical Knowledge in Machine
636 Learning for Ocean Carbon Flux Reconstruction: The pCO₂-Residual Method, Journal of
637 Advances in Modeling Earth Systems, 14(10), <https://doi.org/10.1029/2021ms002960>, 2022a.

638 Bennington, V., Gloege, L., and McKinley, G. A.: Variability in the global ocean carbon sink from
639 1959 to 2020 by correcting models with observations, Geophysical Research Letters, 49(14),
640 <https://doi.org/10.1029/2022GL098632>, (2022b).

641 Bushinsky, S. M., Landschützer, P., Rödenbeck, C., Gray, A. R., Baker, D., Mazloff, M. R.,
642 Resplandy, L., Johnson, K. S., and Sarmiento, J. L.: Reassessing Southern Ocean air-sea CO₂ flux
643 estimates with the addition of biogeochemical float observations, Global Biogeochemical Cycles,
644 33(11), 1370-1388, <https://doi.org/10.1029/2019GB006176>, 2019.

645 Chen, T., and Guestrin, C.: Xgboost: A scalable tree boosting system, In: Proceedings of the 22nd
646 ACM SIGKDD international conference on knowledge discovery and data mining (pp. 785-794),
647 <https://doi.org/10.1145/2939672.2939785>, 2016.

648 Deser, C., Phillips, A., Bourdette, V., and Teng, H.: Uncertainty in climate change projections: the
649 role of internal variability, Climate Dynamics, 38, 527-546, [https://doi.org/10.1007/s00382-010-](https://doi.org/10.1007/s00382-010-0977-x)
650 [0977-x](https://doi.org/10.1007/s00382-010-0977-x), 2012

651 Djetchouang, L. M., Chang, N., Gregor, L., Vichi, M., and Monteiro, P. M. S.: The sensitivity of
652 pCO₂ reconstructions to sampling scales across a Southern Ocean sub-domain: a semi-idealized
653 ocean sampling simulation approach, Biogeosciences, 19, 4171-4195, [https://doi.org/10.5194/bg-](https://doi.org/10.5194/bg-19-4171-2022)
654 [19-4171-2022](https://doi.org/10.5194/bg-19-4171-2022), 2022

655 Fay, A. R., Lovenduski, N. S., McKinley, G. A., Munro, D. R., Sweeney, C., Gray, A. R.,
656 Landschützer, P., Stephens, B. B., Takahashi, T., and Williams, N.: Utilizing the Drake Passage
657 Time-series to understand variability and change in subpolar Southern Ocean pCO₂,
658 Biogeosciences, 15(12), 3841-3855, <https://doi.org/10.5194/bg-15-3841-2018>, 2018.

659 Fay, A. R., and McKinley, G. A.: Observed regional fluxes to constrain modeled estimates of the
660 ocean carbon sink, *Geophysical Research Letters*, 48(20), <https://doi.org/10.1029/2021GL095325>,
661 2021.

662

663 Friedlingstein, P., O'Sullivan, M., Jones, M. W., Andrew, R. M., Bakker, D. C. E., Hauck, J.,
664 Landschützer, P., Le Quéré, C., Luijkx, I. T., Peters, G. P., Peters, W., Pongratz, J., Schwingshackl,
665 C., Sitch, S., Canadell, J. G., Ciais, P., Jackson, R. B., Alin, S. R., Anthoni, P., Barbero, L., Bates,
666 N. R., Becker, M., Bellouin, N., Decharme, B., Bopp, L., Brasika, I. B. M., Cadule, P.,
667 Chamberlain, M. A., Chandra, N., Chau, T.-T.-T., Chevallier, F., Chini, L. P., Cronin, M., Dou,
668 X., Enyo, K., Evans, W., Falk, S., Feely, R. A., Feng, L., Ford, D. J., Gasser, T., Ghattas, J.,
669 Gkritzalis, T., Grassi, G., Gregor, L., Gruber, N., Gürses, Ö., Harris, I., Hefner, M., Heinke, J.,
670 Houghton, R. A., Hurtt, G. C., Iida, Y., Ilyina, T., Jacobson, A. R., Jain, A., Jarníková, T., Jersild,
671 A., Jiang, F., Jin, Z., Joos, F., Kato, E., Keeling, R. F., Kennedy, D., Klein Goldewijk, K., Knauer,
672 J., Korsbakken, J. I., Körtzinger, A., Lan, X., Lefèvre, N., Li, H., Liu, J., Liu, Z., Ma, L., Marland,
673 G., Mayot, N., McGuire, P. C., McKinley, G. A., Meyer, G., Morgan, E. J., Munro, D. R., Nakaoka,
674 S.-I., Niwa, Y., O'Brien, K. M., Olsen, A., Omar, A. M., Ono, T., Paulsen, M., Pierrot, D., Pockock,
675 K., Poulter, B., Powis, C. M., Rehder, G., Resplandy, L., Robertson, E., Rödenbeck, C., Rosan, T.
676 M., Schwinger, J., Séférian, R., Smallman, T. L., Smith, S. M., Sospedra-Alfonso, R., Sun, Q.,
677 Sutton, A. J., Sweeney, C., Takao, S., Tans, P. P., Tian, H., Tilbrook, B., Tsujino, H., Tubiello, F.,
678 van der Werf, G. R., van Ooijen, E., Wanninkhof, R., Watanabe, M., Wimart-Rousseau, C., Yang,
679 D., Yang, X., Yuan, W., Yue, X., Zaehle, S., Zeng, J., and Zheng, B.: Global Carbon Budget 2023,
680 *Earth Syst. Sci. Data*, 15, 5301–5369, <https://doi.org/10.5194/essd-15-5301-2023>, 2023.

681 Fyfe, J. C., Derksen, C., Mudryk, L., Flato, G. M., Santer, B. D., Swart, N. C., Molotch, N. P.,
682 Zhang, X., Wan, H., Arora, V. K., Scinocca, J., and Jiao, Y.: Large near-term projected snowpack
683 loss over the western United States, *Nature communications*, 8(1), 14996,
684 <https://doi.org/10.1038/ncomms14996>, 2017.

685 Gloege, L., McKinley, G. A., Landschützer, P., Fay, A. R., Frolicher, T. L., and Fyfe, J. C.:
686 Quantifying Errors in Observationally Based Estimates of Ocean Carbon Sink Variability, *Global*
687 *Biogeochemical Cycles*, 35(4), <https://doi.org/10.1029/2020gb006788>, 2021.

688 Gloege, L., Yan, M., Zheng, T. and McKinley, G. A.: Improved quantification of ocean carbon
689 uptake by using machine learning to merge global models and pCO₂ data, *Journal of Advances in*
690 *Modeling Earth Systems*, 14(2), <https://doi.org/10.1029/2021MS002620>, 2022.

691

692 Good, S. A., Martin, M., and Rayner, N. A.: EN4: Quality controlled ocean temperature and
693 salinity profiles and monthly objective analyses with uncertainty estimates, *Journal of*
694 *Geophysical Research Oceans*, 118(12), 6704-6717, <https://doi.org/10.1002/2013JC009067>,
695 2013.

696

697 Gray, A. R., Johnson, K. S., Bushinsky, S. M., Riser, S. C., Russell, J. L., Talley, L. D.,
698 Wanninkhof, R., Williams, N. L., and Sarmiento, J. L.: Autonomous biogeochemical floats detect
699 significant carbon dioxide outgassing in the high-latitude Southern Ocean, *Geophysical Research*
700 *Letters*, 45(17), 9049-9057, <https://doi.org/10.1029/2018GL078013>, 2018.

701 Gregor, L., Lebehot, A. D., Kok, S., and Monteiro, P. M. S.: A comparative assessment of the
702 uncertainties of global surface ocean CO₂ estimates using a machine-learning ensemble (CSIR-
703 ML6 version 2019a) – have we hit the wall?, *Geoscientific Model Development*, 12, 5113-5136,
704 <https://doi.org/10.5194/gmd-12-5113-2019>, 2019.

705 Gregor, L. and Fay, A. R.: Air-sea CO₂ fluxes for surface pCO₂ data products using a standardized
706 approach, Zenodo [code], <https://doi.org/10.5281/zenodo.5482547>, 2021.

707 Gruber, N., Landschützer, P., and Lovenduski, N. S.: The variable Southern Ocean carbon sink,
708 *The Annual Review of Marine Science*, 11, 159-86, [https://doi.org/10.1146/annurev-marine-](https://doi.org/10.1146/annurev-marine-121916-063407)
709 [121916-063407](https://doi.org/10.1146/annurev-marine-121916-063407), 2019.

710 Hauck, J., Nissen, C., Landschützer, P., Rödenbeck, C., Bushinsky, S., and Olsen, A.: Sparse
711 observations induce large biases in estimates of the global ocean CO₂ sink: and ocean model
712 subsampling experiment, *Philosophical Transactions Of the Royal Society A*, 381:20220063,
713 <https://doi.org/10.1098/rsta.2022.0063>, 2023.

714 Kay, J. E., Deser, C., Phillips, A., Mai, A., Hannay, C., Strand, G., Arblaster, J. M., Bates, S. C.,
715 Danabasoglu, G., Edwards, J., Holland, M., Kushner, P., Lamarque, J-F., Lawrence, D., Lindsay,
716 K., Middelton, A., Munoz, E., Nealse, R., Oleson, K., Polvani, L., and Vertenstein, M.: The

717 Community Earth System Model (CESM) large ensemble project: A community resource for
718 studying climate change in the presence of internal climate variability, *Bulletin of the American*
719 *Meteorological Society*, 96(8), 1333-1349, <https://doi.org/10.1175/BAMS-D-13-00255>, 2015.

720 Khatiwala, S., Primeau, F., and Hall, T.: Reconstruction of the history of anthropogenic CO₂
721 concentrations in the ocean, *Nature*, 462(7271), 346-349, <https://doi.org/10.1038/nature08526>,
722 2009.

723 Landschützer, P., Gruber, N., Bakker, D. C. E., and Schuster, U.: Recent variability of the global
724 ocean carbon sink, *Global Biogeochemical Cycles*, 28(9), 927-949,
725 <https://doi.org/10.1002/2014GB004853>, 2014.

726 Landschützer, P., Gruber, N., Haumann, F. A., Rödenbeck, C., Bakker, D. C. E., Van Heuven, S.,
727 Hoppema, M., Metzl, N., Sweeney, C., Takahashi, T., Brook, B., and Wanninkhof, R.: The
728 reinvigoration of the Southern Ocean carbon sink, *Science*, 349(6253), 1221-1224,
729 <https://doi.org/10.1126/science.aab2620>, 2015.

730 Landschützer, P., Tanhua, T., Behncke, J., and Keppler, L.: Sailing through the Southern Ocean
731 seas of air-sea CO₂ flux uncertainty, *Philosophical Transactions of the Royal Society A*, 381,
732 <https://doi.org/10.1098/rsta.2022.0064>, 2023.

733 Lenton, A. B., Matear, R. J., and Tilbrook, B.: Design of an observational strategy for quantifying
734 the Southern Ocean uptake of CO₂, *Global Biogeochemical Cycles*, 20, 1-11.
735 <https://doi.org/10.1029/2005GB002620>, 2006.

736 Lenton, A. B., Tilbrook, B., Law, R. M., Bakker, D. C. E., Doney, S. C., Gruber, N., Ishii, M.,
737 Hoppema, M., Lovenduski, N. S., Matear, R. J., McNeil, B. I., Metzl, N., Mikaloff Fletcher, S. E.,
738 Monteiro, P. M. S., Rödenbeck, C., Sweeney, C., and Takahashi, T.: Sea-air CO₂ fluxes in the
739 Southern Ocean for the period 1990-2009, *Biogeosciences*, 10, 4037-4054,
740 <https://doi.org/10.5194/bg-10-4037-2013>, 2013.

741 Le Quéré, C., Rödenbeck, C., Buitenhuis, E. T., Conway, T. J., Lagenfelds, R., Gomez, A.,
742 Labuschagne C., Ramonet, M., Nakazawa, T., Metzl, N., Gillett, N., and Heimann, M.: Saturation
743 of the Southern Ocean CO₂ sink due to recent climate change, *Science*, 316(5832), 1735-1738,
744 <https://doi.org/10.1126/science.1136188>, 2007.

745 Long, M. C., Stephens, B. B., McKain, K., Sweeney, C., Keeling, R. F., Kort, E. A., Morgan, E.
746 J., Bent, J. D., Chandra, N., Chevallier, F., Commane, R., Daube, B. C., Krummel, P. B., Loh, Z.,
747 Lujikx, I. T., Munro, D., Patra, P., Peters, W., Ramonet, M., Rödenbeck, C., Stavert, A., Tans, P.,
748 and Wofsy, S. C.: Strong Southern Ocean carbon uptake evident in airborne observations, *Science*,
749 374(6572), 1275-1280, <https://doi.org/10.1126/science.abi4355>, 2021.

750 Mackay, N., and Watson, A.: Winter air-sea CO₂ fluxes constructed from summer observations of
751 the polar Southern Ocean suggest weak outgassing, *Journal of Geophysical Research: Oceans*,
752 126(5), e2020JC016600, <https://doi.org/10.1029/2020JC016600>, 2021.

753 Mackay, N., Watson, A., Suntharalingam, P., Chen, Z., and Rödenbeck, C.: Improved winter data
754 coverage of the Southern Ocean CO₂ sink from extrapolation of summertime observations,
755 *Communications Earth & Environment*, 3, 265, <https://doi.org/10.1038/s43247-022-00592-6>,
756 2022.

757 McKinley, G. A., Fay, A. R., Eddebbar, Y. A., Gloege, L., and Lovenduski, N. S.: External forcing
758 explains recent decadal variability of the ocean carbon sink, *AGU Advances*, 1(2),
759 e2019AV000149, <https://doi.org/10.1029/2019AV000149>, 2020.

760 Mongwe, N. P., Vichi, M., and Monteiro, P. M. S.: The seasonal cycle of *p*CO₂ and CO₂ fluxes in
761 the Southern Ocean: diagnosing anomalies in CMIP5 Earth system models, *Biogeosciences*, 15(9),
762 2851-2872, <https://doi.org/10.5194/bg-15-2851-2018>, 2018.

763 Monteiro, P. M. S., Gregor, L., Lévy, M., Maenner, S., Sabine, C. L., and Swart, S.: Intraseasonal
764 variability linked to sampling alias in air-sea CO₂ fluxes in the Southern Ocean, *Geophysical*
765 *Research Letters*, 42(20), 8507-8514, <https://doi.org/10.1002/2015GL066009>, 2015.

766 Rodgers, K. B., Lin, J., and Frölicher, T. L.: Emergence of multiple ocean ecosystem drivers in a
767 large ensemble suite with an Earth system model, *Biogeosciences*, 12(11), 3301-3320.
768 <https://doi.org/10.5194/bg-12-3301-2015>, 2015.

769 Rödenbeck, C., Bakker, D. C. E., Gruber, N., Iida, Y., Jacobson, A. R., Jones, S., Landschützer,
770 P., Metzl, N., Nakaoka, S., Olsen, A., Park, G.-H., Peylin, P., Rodgers, K. B., Sasse T. P., Schuster,
771 U., Shutler, J. D., Valsala, V., Wannikhhof, R., and Zeng, J.: Data-based estimates of the ocean

772 carbon sink variability – first results of the Surface Ocean $p\text{CO}_2$ Mapping intercomparison
773 (SOCOM), *Biogeosciences*, 12, 7251-7278, <https://doi.org/10.5194/bg-12-7251-2015>, 2015.

774 Sabine, C., Sutton, A., McCabe, K., Lawrence-Slavas, N., Alin, S., Feely, R., Jenkins, R., Maenner,
775 S., Meinig, C., Thomas, J., van Ooijen, E., Passmore, A., and Tilbrook, B.: Evaluation of a new
776 carbon dioxide system for autonomous surface vehicles, *Journal of Atmospheric and Oceanic*
777 *Technology*, 37(8), 1305-1317, <https://doi.org/10.1175/JTECH-D-20-0010.1>, 2020.

778 Stamell, J., Rustagi, R. R., Gloege, L., and McKinley, G. A.: Strengths and weaknesses of three
779 Machine Learning methods for $p\text{CO}_2$ interpolation, *Geoscientific Model Development*
780 *Discussions*[preprint], doi:10.5194/gmd-2020-311, 22 October 2020.

781 Sutton, A. J., Williams, N. L., and Tilbrook, B.: Constraining Southern Ocean CO_2 flux uncertainty
782 using uncrewed surface vehicle observations, *Geophysical Research Letters*, 48(3),
783 e2020GL091748, <https://doi.org/10.1029/2020GL091748>, 2021.

784 Takahashi, T., Olafsson, J., Goddard, J. G., Chipman, D. W., and Sutherland, S. C.: Seasonal
785 variation of CO_2 and nutrients in the high-latitude surface oceans: A comparative study, *Global*
786 *Biogeochemical Cycles*, 7(4), 843-878, <https://doi.org/10.1029/93GB02263>, 1993.

787 Takahashi, T., Sutherland, S. C., Wanninkhof, R., Sweeney, C., Feely, R. A., Chipman, D. W.,
788 Hales, B., Friederich, G., Chavez, F., Sabine, C., Watson, A., Bakker, D. C. E., Schuster, U., Metzl,
789 N., Yoshikawa-Inoue, H., Ishii, M., Midorikawa, T., Nojiri, Y., Körtzinger, A., Steinhoff, T.,
790 Hoppema, M., Olafsson, J., Arnarson, T. S., Tilbrook, B., Johannessen, T., Olsen, A., Bellerby,
791 R., Wong, C. S., Delille, B., Bates, N. R., and de Baar, H. J. W.: Climatological mean and decadal
792 change in surface ocean $p\text{CO}_2$, and net sea-air CO_2 flux over the global oceans, *Deep Sea Research*
793 *Part II: Topical Studies in Oceanography*, 56(8-10), 554-557,
794 <https://doi.org/10.1016/j.dsr2.2008.12.009>, 2009.

795 Toms, B. A., Barnes, E. A., and Ebert-Uphoff, I.: Physically interpretable neural networks for the
796 geosciences: Applications to earth system variability, *Journal of Advances in Modeling Earth*
797 *Systems*, 12(9), e2019MS002002, <https://doi.org/10.1029/2019MS002002>, 2020.

798 Williams, N. L., Juranek, L. W., Feely, R. A., Johnson, K. S., Sarmiento, J. L., Talley, L. D.,
799 Dickson, A. G., Gray, A. R., Wanninkhof, R., Russell, J. L., Riser, S. C., and Takeshita, Y.:

800 Calculating surface ocean pCO₂ from biogeochemical Argo floats equipped with pH: An
801 uncertainty analysis, *Global Biogeochemical Cycles*, 31(3), 591-604,
802 <https://doi.org/10.1002/2016GB005541>, 2017.

803 Wu, Y., Bakker, D. C. E., Achterberg, E. P., Silva, A. N., Pickup D. P., Li, X., Hartman, S.,
804 Stappard, D., Qi, D., and Tyrrell, T.: Integrated analysis of carbon dioxide and oxygen
805 concentrations as a quality control of ocean float data, *Communications Earth & Environment*, 3,
806 92, <https://doi.org/10.1038/s43247-022-00421-w>, 2022.

807

808

809

810

811

812